(article starts on next page)

Contents lists available at ScienceDirect

International Journal of Solids and Structures

Computational homogenization for predicting the effective response of planar textile-reinforced concrete shells

Gabriel Edefors [a,b] [ID],[*], Fredrik Larsson [b] [ID], Karin Lundgren [a] [ID]

[a] *Department of Architecture and Civil Engineering, Chalmers University of Technology, Gothenburg, 41258, Sweden*
[b] *Department of Industrial and Materials Science, Chalmers University of Technology, Gothenburg, 41258, Sweden*

ARTICLE INFO

ABSTRACT

Textile-reinforced concrete (TRC) exhibits a complex mechanical response, necessitating accurate and advanced models for analysis. This work shows the possibilities to model TRC using a two-scale approach. On the sub-scale, the response is predicted using Representative Volume Elements (RVEs), where the textile yarns are resolved. This approach makes it possible to capture the effects of bond–slip, interfilament slip, as well as concrete cracking and crushing. The large-scale plate response, in terms of membrane forces and bending moments, is obtained by homogenizing the results from the RVE using Kirchhoff plate kinematics. The outcome shows the possibilities of obtaining effective large-scale responses for varying sub-scale configurations. In this way, we omit the need for re-calibrating the large-scale model for every new reinforcement configuration. The scale-bridging framework developed in this work can be employed in large-scale plate and shell models to predict the effective constitutive response of TRC.

1. Introduction

Textile-reinforced concrete (TRC) is an emerging composite material with potential as an efficient alternative to steel reinforced concrete (Brameshuber, 2006). Unlike steel, the textile fibers used are not susceptible to corrosion, eliminating the need for a passivating concrete cover and reducing the total amount of required concrete. In general, TRC performs well in the serviceability state, where the fine reinforcement mesh results in a favorable crack pattern with many small cracks (Preinstorfer et al., 2019). Moreover, TRC can be used for curved structures since the flexible textiles easily can be bent. This capability opens up the possibility of manufacturing for instance lightweight ceiling systems using curved shells as in May et al. (2018). TRC has also been demonstrated for use in lightweight low-maintenance bridges (Helbig et al., 2016). While TRC has been demonstrated to have properties that make it an appealing alternative to steel reinforcement for many applications, its widespread adoption remains limited. One reason for this is the lack of knowledge of the mechanical behavior of TRC (Preinstorfer et al., 2023), such as stress redistribution and strain softening due to matrix cracking and yarn debonding (Sharei et al., 2017). Moreover, since TRC exhibits less ductility than conventional reinforced concrete, it is paramount to base the design on a realistic stress distribution, since stress redistribution is limited (Yu et al., 2021). Consequently, there is a necessity for accurate non-linear mechanical models that describe the complex response for various loading conditions. The complex behavior of TRC stems from the interaction between the reinforcement yarns and the concrete and cracking of the concrete (Chudoba et al., 2016). Unlike steel reinforcement, where the bars have a uniform stress, the stress in the yarns is non-uniform due to interfilament slip. This interfilament slip, which also leads to partial activation of the inner filaments, can be modeled with efficiency factors for strength and stiffness as in (Hegger and Voss, 2008; Sciegaj et al., 2022). These factors vary between 1 for full activation and 0 for no activation of the filaments.

Several authors have addressed the influence of the sub-scale composition on large-scale behavior. One approach is to use multi-scale modeling to account for the sub-scale heterogeneities. In short, multi-scale modeling acknowledges the fact that the effective response of a material is determined from phenomena that occur on multiple different smaller length scales. To this end, the material is modeled on different length scales, capturing different phenomena, and then coarse-grained to obtain an effective response at the larger length scales (Geers et al., 2010). The coarse-graining, often referred to as homogenization, is typically based on some kind of averaging of the response on the smaller scales, either by analytical or numerical methods. By using computational homogenization, it is possible to capture the response of complex sub-structures without having to use restrictive assumptions as when using analytical homogenization (Yvonnet, 2019). Typically,

---

since the response on the different scales is dependent on the response on the other scales, the problem has to be solved concurrently. One popular such approach is the FE^2 method, where each integration point in the large-scale mesh is associated with a Representative Volume Element (RVE). For each load step, the solution on the large scale is sent to the sub-scale and applied as boundary conditions to the RVE. Subsequently, the solution from the RVE is homogenized and sent back to the large scale (Feyel and Chaboche, 2000). A drawback of computational homogenization is its computational expense, as concurrent analyses must be performed at multiple length scales. However, this can somewhat be compensated by solving the sub-scale problems in parallel (Coenen et al., 2010). An example of a multi-scale modeling approach using Eshelby's solution for TRC can be found in Richter (2005). The major advantage of such an analytical homogenization model lies in its simplicity and ability to capture sub-scale features efficiently. Some disadvantages however, as pointed out by the author, are that such a model is restricted to relatively simple sub-scale configurations, constitutive models and boundary conditions. A similar model developed by Zastrau et al. (2008) is the hierarchical multi-scale framework, that can be used to model TRC on three different length scales, predetermining the scale transition before the simulation. Another modeling approach that has been used is the semi-smeared layered type of model, where the influence of each reinforcement layer is smeared in the plane and then stacked with plain concrete layers to form a composite cross layup, see e.g. Kadi et al. (2018). Although this approach has demonstrated overall accuracy, it presents certain drawbacks. Specifically, the material response of the reinforcement layer must be re-calibrated whenever the reinforcement configuration changes. Additionally, the smeared representation of the reinforcement means that the dependency between crack spacing and yarn spacing, and local effects, such as yarn pullout, cannot be accurately captured.

While homogenization primarily has been used to scale up the response in a general 3D setting, work has been done to scale up the response to effective structural members such as beams, plates and shells. In particular, methods for scaling up the response to planar shells using Kirchhoff–Love kinematics have been developed in e.g. Geers et al. (2010), Mercatoris and Massart (2011), Challagulla et al. (2008) and Oskay and Pal (2010), with the latter two employing asymptotic homogenization to derive effective properties. Similarly, methods for scaling up the response to thick shells using Reissner–Mindlin kinematics have been developed, e.g. in Coenen et al. (2010) and Petracca et al. (2017). A consistent method of deriving the multi-scale problem from the single-scale problem, denoted Variationally Consistent Homogenization (VCH), was developed in Larsson et al. (2010) and has been applied by Sciegaj et al. (2020) to model steel-reinforced concrete using Kirchhoff–Love kinematics and by Börjesson et al. (2023) to model composites using Reissner–Mindlin kinematics. Another approach to account for the sub-scale damage and anisotropy of TRC is the micro-plane damage model, which makes it possible to use a homogeneous shell representation of TRC at the large-scale (Chudoba et al., 2016; Platen et al., 2023). However, this model requires re-calibration when the cross-section layout or reinforcement configuration is changed.

Although most aspects of the modeling of TRC have been considered through a variety of different analytical and numerical methods, there is still a need of a comprehensive computational framework for the analysis of arbitrary large-scale TRC plate and shell structures. In this paper, we propose, as a first step in such a modeling framework, an upscaling framework from the sub scale RVE to the large scale effective homogeneous Kirchhoff–Love plate. Currently, only planar textiles are considered, meaning that yarns are assumed to be straight. However, no restrictions are imposed on their orientation or length, hence the proposed technique could be used to model simple 3D textiles. This framework considers concrete cracking and crushing, bond–slip, and interfilament slip on the sub-scale and only requires calibration on the sub-scale. The developed upscaling approach is suited for accurately modeling large-scale plate and shell structures without having to fully resolve all sub-scale features. At the sub-scale, we model TRC using RVEs, where we resolve the yarns and the interface with the concrete. The upscaling to the large-scale plate model follows the approach in Sciegaj et al. (2020), where the effective-plate membrane forces and bending moments are obtained by employing a homogenization scheme based on the Kirchhoff–Love plate kinematics. Although the upscaling in this work is done for plates, it could be used to model shells by using planar facet shell elements. The motivation for choosing a two-scale modeling approach is twofold. Firstly, we note that the overall response of TRC is heavily influenced by the sub-scale composition and behavior (Rampini et al., 2019). By modeling TRC on the finer sub-scale, we can employ a bond–slip model that captures the complex yarn-concrete interaction (Sciegaj et al., 2022). Secondly, we acknowledge that it is infeasible to model large-scale structures with fully resolved models (Unger and Eckardt, 2011).

The remainder of this paper is organized as follows: Section 2 describes the mechanical model used for modeling TRC on the sub-scale. This includes the approximation of the yarn and the interface between the yarn and the concrete as well as the formulation of the weak problem for equilibrium of the yarns and the concrete. Section 3 treats the two-scale modeling using VCH and the associated prolongation and homogenization operators used. Based on this, the sub-scale and large-scale problems are derived. In Section 4, the material models and parameters used for the numerical studies are presented. In Section 5, the upscaling framework is validated and then used to demonstrate how effective large-scale moment–curvature and strain-membrane force relations can be obtained. Also, the influence of RVE size and different boundary conditions is investigated. Finally, the results and suggestions for further work are discussed in Section 6.

2. Modeling of textile-reinforced concrete

This section outlines the modeling approach for the yarns, the concrete, and the interface between them. The starting point is a fully resolved 3D representation of the yarns. From this, certain approximations and the introduction of efficiency factors for strength and stiffness allow us to idealize the response of the yarns as functions of their centerline coordinate. Additionally, we account for the weakening effect by reducing the concrete's stiffness, strength, and fracture energy in proportion to the volume occupied by the yarns. The concrete is modeled as a continuum, and damage is accounted for using an isotropic damage model. Finally, the equilibrium equations are established in both the strong and weak form.

2.1. Idealization of the yarns

Consider a textile yarn composed of multiple filaments that occupy the domain Ω_r, with the longitudinal coordinate $l \in \Gamma_r$ passing through the centroid. The boundary of the yarn is divided into a lateral part $\partial\Omega_{r,lat}$ surrounding the yarn and a part $\partial\Omega_{r,end}$ at the yarn's ends, such that $\partial\Omega_r = \partial\Omega_{r,lat} \cup \partial\Omega_{r,end}$, see Fig. 1. An arbitrary cross-section of the yarn is denoted A_r and the associated boundary is denoted ∂A_r. The yarn is considered to be homogeneous, with the displacement field $\bar{u}_r(\hat{x}, l)$ and the stress field $\bar{\sigma}_r(\hat{x}, l)$, for $\hat{x} \in A_r$. For an arbitrary point $x \in \bar{\Omega}_r$, we define x_r as the closest point on Γ_r, i.e.

$$x_r(x) := \arg\min_{\hat{x}_r \in \Gamma_r} \|x - \hat{x}_r\|. \tag{1}$$

Using this definition, it is now possible to approximate the yarn displacement $\bar{u}_r$ as the displacement at $x_r(x)$

$$\bar{u}_r(x) \approx u_r(x_r(x)), \tag{2}$$
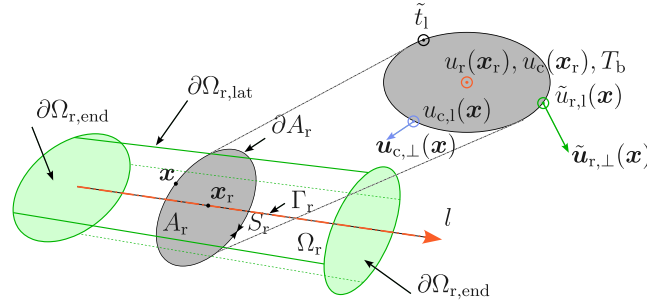
where u_r is only defined on Γ_r.

Fig. 1. Cut-out of a textile yarn showing the displacement and stress fields.

2.1.1. Normal force in the yarn

Following the approach in Richter (2005), the yarn is assumed not to transfer any normal or shear stresses in the transverse direction. Moreover, the bending stiffness of the yarn is assumed to be small. As a consequence, it suffices to consider only the normal stress component along the yarn $\tilde{\sigma}_r := \tilde{\sigma}_r : [e_l \otimes e_l]$. From this, the normal force in an arbitrary cross-section of the yarn is obtained as

$$N_r = \int_{A_r} \tilde{\sigma}_r \ \mathrm{d}A = A_r \sigma_r \left(\boldsymbol{x}_r \right), \tag{3}$$

where the normal stress $\tilde{\sigma}_r$ is represented by its average $\sigma_r \left(\boldsymbol{x}_r \right)$ defined on Γ_r, see Fig. 2. The yarns are assumed to have a linear elastic response, even though the yarns exhibit a non-linear behavior at low strains due to the straightening of the filaments (Bruckermann, 2007), and progressive failure at high strains (Bruckermann, 2007; Krüger, 2004). This approximation has proven to be sufficient for modeling the response of TRC (Sciegaj et al., 2023). Using this assumption of linear elasticity, the varying normal stress $\tilde{\sigma}_r$ in the yarn can be related to the varying normal strain $\tilde{\varepsilon}_r$ using the nominal stiffness E_r^0 (the stiffness of a single filament) and the uniform normal stress σ_r can be related to the uniform normal strain ε_r using the effective stiffness E_r respectively, i.e.

$$\tilde{\sigma}_r = E_r^0 \tilde{\varepsilon}_r, \quad \tilde{\varepsilon}_r := [\tilde{\boldsymbol{u}}_r \otimes \nabla] : [e_l \otimes e_l] \tag{4a}$$

$$\sigma_r = E_r \varepsilon_r, \quad \varepsilon_r := \frac{\mathrm{d}u_r}{\mathrm{d}l} \tag{4b}$$

where $u_r = \boldsymbol{u}_r \cdot e_l$ is the longitudinal component of the uniform yarn displacement. By inserting Eqs. (4a) and (4b) in Eq. (3), one obtains the relation between the nominal and the effective stiffness

$$E_r = \eta_E E_r^0, \quad \eta_E := \frac{\frac{1}{A_r} \int_{A_r} \tilde{\varepsilon}_r \ \mathrm{d}A}{\varepsilon_r} \tag{5}$$

where η_E is assumed to be a constant efficient factor. Moreover, we define that failure of the yarn occurs when the most stressed filament reaches the nominal strength f_u^0, i.e. the strength of a single filament. Equivalently, the effective failure stress f_u can be related to the uniform stress σ_r

$$\max_{\hat{\boldsymbol{x}} \in A_r} \tilde{\sigma}_r(\hat{\boldsymbol{x}}, l) = f_u^0, \tag{6a}$$

$$\sigma_r = f_u \tag{6b}$$

By combining these failure criteria, together with Eq. (3), it is possible to relate the uniaxial strength of the yarn f_u and the nominal strength of a single filament f_u^0 as

$$f_u = \eta_f f_u^0, \quad \eta_f = \frac{\frac{1}{A_r} \int_{A_r} \tilde{\sigma}_r \ \mathrm{d}A}{\max_{\hat{\boldsymbol{x}} \in A_r} \tilde{\sigma}_r(\hat{\boldsymbol{x}})}. \tag{7}$$

This strength efficiency factor η_f can be identified as the same one used in e.g. as in Peled and Bentur (2000). Note that both η_E and η_f have to be determined from experimental testing.
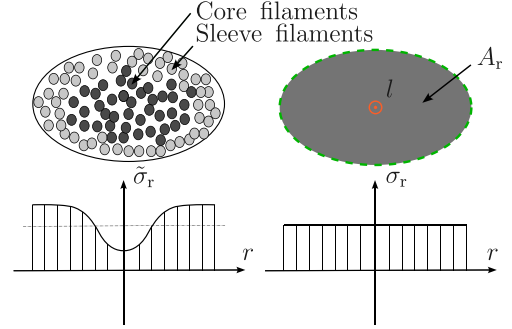

Fig. 2. Idealization of the normal stress in a cross-section of a yarn.

2.1.2. Compatibility between yarn and concrete

The yarn is assumed to be rigidly coupled to the concrete in the transverse direction, which in general can be expressed as

$$\boldsymbol{u}_{r,\perp}(\boldsymbol{x}_r(\boldsymbol{x})) = \boldsymbol{u}_{c,\perp}(\boldsymbol{x}) \text{ on } \partial \Omega_{r,\text{lat}}, \tag{8}$$

where $\boldsymbol{u}_{r,\perp} = [\boldsymbol{I} - e_l \otimes e_l] \cdot \boldsymbol{u}_r$ and $\boldsymbol{u}_{c,\perp} = [\boldsymbol{I} - e_l \otimes e_l] \cdot \boldsymbol{u}_c$ are the transverse displacement components of the yarn and the concrete respectively. The yarn is however allowed to slip relative to the concrete in the longitudinal direction. The slip, generally varying around the perimeter of the yarn $\partial \Omega_{r,\text{lat}}$, between the concrete and the yarn is defined as the relative displacement in the longitudinal direction, i.e.

$$\tilde{s}_l(\boldsymbol{x}) = u_r(\boldsymbol{x}_r(\boldsymbol{x})) - u_{c,l}(\boldsymbol{x}) \text{ on } \partial \Omega_{r,\text{lat}}, \tag{9}$$

where $u_{c,l} = \boldsymbol{u}_c \cdot e_l$ is the longitudinal projection of the concrete displacement, and as we recall $u_r = \boldsymbol{u}_r \cdot e_l$. The bond–slip in the longitudinal direction gives rise to a conjugate longitudinal traction component $\tilde{t}_{b,l}(\tilde{s}_l) = \tilde{t}_b \cdot e_l$ between the concrete and the reinforcement yarn, where $\tilde{t}_b$ is the traction between the concrete and the yarn. Note that the transverse component $\tilde{t}_{b,\perp} = [\boldsymbol{I} - e_l \otimes e_l] \cdot \tilde{t}_b$ is the reaction stress associated to the constraint in Eq. (8). $\tilde{t}_{b,l}$ can be integrated along the perimeter of the yarn to obtain the bond-force per unit length T_b, i.e.

$$T_b(\tilde{s}_l) = \int_{\partial A_r} \tilde{t}_{b,l}(\tilde{s}_l) \ \mathrm{d}S \tag{10}$$

2.2. Concrete stress

To account for damage caused by cracking and crushing, an isotropic damage model referred to as the Mazars model is employed (Mazars, 1986). In such a model, the damaged concrete stress σ_c is expressed as a degradation of the elastic stress $\sigma_{c,0}$, using the damage variable d, such as

$$\sigma_c = (1 - d)\sigma_{c,0}\left(\boldsymbol{u}_c\right). \tag{11}$$

The damage parameter d equals 0 when no damage has occurred and 1 for complete damage. For further details about the damage
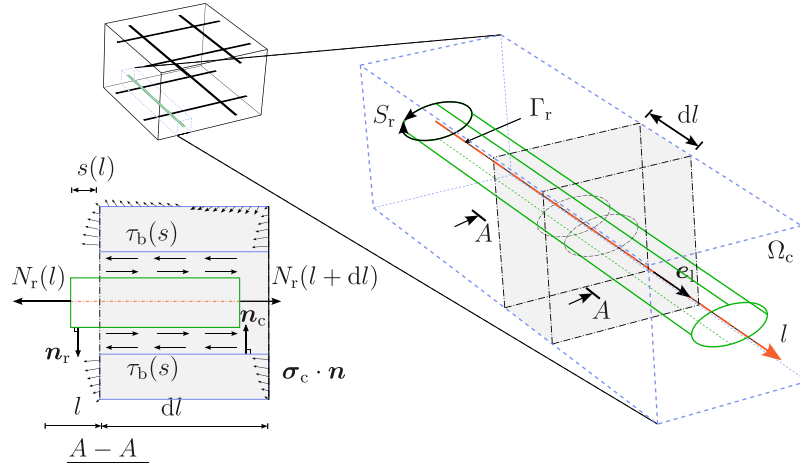
Fig. 3. Cut-out of a TRC-body, showing a yarn, the surrounding concrete, and the interface in between the yarn and the concrete.
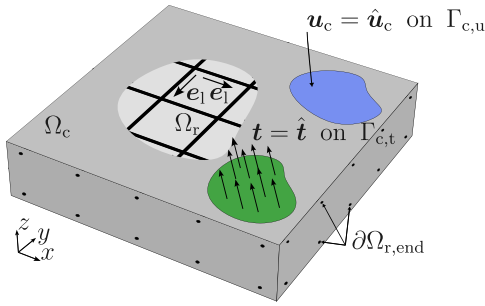

Fig. 4. Single-scale TRC-problem with the different domains and displacement fields.

modeling, see Appendix E. Spatial regularization is done using the crack-band method, whereby the strain is assumed to localize over a width h_{cb}.

2.3. Equilibrium equations

Now, consider a textile-reinforced concrete body, occupying the domain Ω, see Fig. 4. The reinforcement yarns occupy Ω_r, inside the concrete domain Ω_c, such that $\Omega = \Omega_c \cup \Omega_r$. The displacement field associated with the concrete is denoted $\boldsymbol{u}_c$ and has three components. The boundary of Ω_c can be divided into a part with prescribed traction $\Gamma_{c,t}$, a part with prescribed displacement $\Gamma_{c,u}$ and a part that constitutes the lateral interface with the yarns $\partial\Omega_{r,lat}$ and a part that constitutes the interface at the ends of the yarns $\partial\Omega_{r,end}$.

2.3.1. Concrete equilibrium

From the above, the strong form of the equilibrium in the concrete domain can be formulated as

$$-\boldsymbol{\sigma}_c \cdot \boldsymbol{\nabla} = \hat{\boldsymbol{b}} \quad \text{in } \Omega_c, \tag{12a}$$

$$\boldsymbol{u}_c = \hat{\boldsymbol{u}}_c \quad \text{on } \Gamma_{c,u}, \tag{12b}$$

$$\boldsymbol{\sigma}_c \cdot \boldsymbol{n}_c = \hat{\boldsymbol{t}} \quad \text{on } \Gamma_{c,t}, \tag{12c}$$

$$\boldsymbol{\sigma}_c \cdot \boldsymbol{n}_c = \tilde{\boldsymbol{t}}_b \quad \text{on } \partial\Omega_{r,lat}, \tag{12d}$$

$$\boldsymbol{\sigma}_c \cdot \boldsymbol{n}_c = \boldsymbol{0} \quad \text{on } \partial\Omega_{r,end} \tag{12e}$$

where $\hat{\boldsymbol{b}}$ is the body load on the concrete, $\hat{\boldsymbol{t}}$ is a prescribed traction vector, $\hat{\boldsymbol{u}}_c$ is a prescribed displacement vector and $\tilde{\boldsymbol{t}}_b$ is the boundary traction vector acting on the concrete and $\boldsymbol{n}_c$ is the outwards pointing

unit normal of the concrete, see Fig. 3. The corresponding weak form of (12a) can be expressed as

$$\int_{\Omega_c} \boldsymbol{\sigma}_c : [\delta\boldsymbol{u}_c \otimes \boldsymbol{\nabla}] \ d\Omega - \int_{\Gamma_r} \int_{\partial A_r} \tilde{t}_{b,l} \ \delta u_{c,l} \ dS \ d\Gamma$$

$$= \int_{\Omega_c} \hat{\boldsymbol{b}} \cdot \delta\boldsymbol{u}_c \ d\Omega + \int_{\Gamma_{c,t}} \hat{\boldsymbol{t}} \cdot \delta\boldsymbol{u}_c \ d\Gamma, \tag{13}$$

where it was used that $\partial\Omega_{r,lat} = \Gamma_r \times \partial A_r$.

2.3.2. Yarn equilibrium

Similarly as for the concrete, the general strong form of the equilibrium of the yarns can be formulated as

$$-\tilde{\boldsymbol{\sigma}}_r \cdot \boldsymbol{\nabla} = 0 \quad \text{in } \Omega_r, \tag{14a}$$

$$\tilde{\boldsymbol{\sigma}}_r \cdot \boldsymbol{n}_r = -\tilde{\boldsymbol{t}}_b \quad \text{on } \partial\Omega_{r,lat}, \tag{14b}$$

$$\tilde{\boldsymbol{\sigma}}_r \cdot \boldsymbol{n}_r = \boldsymbol{0} \quad \text{on } \partial\Omega_{r,end}, \tag{14c}$$

where $\boldsymbol{n}_r$ is the outwards pointing unit normal of the surface of the reinforcement yarns, see Fig. 3. The boundary condition in Eq. (14c) implies that the ends of the yarns are free. At this stage, no Dirichlet boundary conditions have been specified for the yarns. The corresponding weak form of (14a) can be expressed as

$$\int_{\Omega_r} \tilde{\boldsymbol{\sigma}}_r : [\delta\tilde{\boldsymbol{u}}_r \otimes \boldsymbol{\nabla}] \ d\Omega - \int_{\partial\Omega_{r,lat}} [\tilde{\boldsymbol{\sigma}}_r \cdot \boldsymbol{n}_r] \cdot \delta\tilde{\boldsymbol{u}}_r \ dA = 0. \tag{15}$$

Note that Eqs. (14c) was used to get rid of the boundary term related to $\partial\Omega_{r,end}$. By applying the assumption of uniaxial stress and substituting the interface boundary condition in Eqs. (14b) and (15) can be written as

$$\int_{\Gamma_r} \int_{A_r} \tilde{\sigma}_r \frac{d\delta\tilde{u}_r}{dl} \ dA \ d\Gamma + \int_{\Gamma_r} \int_{\partial A_r} \tilde{t}_{b,l} \ dS \ \delta u_r \ d\Gamma = 0. \tag{16}$$

Finally, by using the approximation in Eq. (3), the weak form of the yarn equilibrium can be written as

$$\int_{\Gamma_r} N_r \frac{d\delta u_r}{dl} \ d\Gamma + \int_{\Gamma_r} \int_{\partial A_r} \tilde{t}_{b,l} \ dS \ \delta u_r \ d\Gamma = 0. \tag{17}$$

2.4. Weak form of the single-scale TRC problem

We are now in the position to formulate the weak form of the full TRC problem by combining Eqs. (13) and (17): Find $\boldsymbol{u}_c \in \mathbb{U}_c$ and $u_r \in \mathbb{U}_r$ such that

$$\tilde{a}_c\left(\boldsymbol{u}_c; \delta\boldsymbol{u}_c\right) - \tilde{b}\left(u_r - \boldsymbol{e}_l \cdot \boldsymbol{u}_c; \boldsymbol{e}_l \cdot \delta\boldsymbol{u}_c\right) = l_c\left(\delta\boldsymbol{u}_c\right) \quad \forall \ \delta\boldsymbol{u}_c \in \mathbb{U}_c^0,$$

$$a_r\left(u_r; \delta u_r\right) + \tilde{b}\left(u_r - \boldsymbol{e}_l \cdot \boldsymbol{u}_c; \delta u_r\right) = 0 \quad \forall \ \delta u_r \in \mathbb{U}_r, \tag{18}$$

where the bilinear forms for the concrete and the yarns are defined as

$$\tilde{a}_c \left(\boldsymbol{u}_c; \delta \boldsymbol{u}_c \right) := \int_{\Omega_c} \boldsymbol{\sigma}_c \left(\boldsymbol{\varepsilon}[\boldsymbol{u}_c] \right) : \left[\delta \boldsymbol{u}_c \otimes \boldsymbol{\nabla} \right] \ d\Omega, \tag{19}$$

$$a_r \left(u_r; \delta u_r \right) := \int_{\Gamma_r} N_r \left(\frac{du_r}{dl} \right) \frac{d\delta u_r}{dl} \ d\Gamma, \tag{20}$$

$$\tilde{b} \left(u; \delta v \right) := \int_{\Gamma_r} \int_{\partial A_r} \tilde{t}_{b,l}(u) \ \delta v \ dS \ d\Gamma. \tag{21}$$

Finally, the loading form, containing contributions from both the body load and boundary traction is defined as

$$l_c \left(\delta \boldsymbol{u}_c \right) = \int_{\Gamma_{c,t}} \hat{\boldsymbol{t}} \cdot \delta \boldsymbol{u}_c \ d\Gamma + \int_{\Omega_c} \hat{\boldsymbol{b}} \cdot \delta \boldsymbol{u}_c \ d\Omega. \tag{22}$$

The trial and test spaces are defined as

$$\mathbb{U}_c = \left\{ \boldsymbol{u} \in [\mathbb{H}^1(\Omega_c)]^3, \boldsymbol{u}_c = \hat{\boldsymbol{u}}_c \text{ on } \Gamma_{c,u} \right\}, \tag{23}$$

$$\mathbb{U}_c^0 = \left\{ \boldsymbol{u} \in [\mathbb{H}^1(\Omega_c)]^3, \boldsymbol{u}_c = \boldsymbol{0} \text{ on } \Gamma_{c,t} \right\}, \tag{24}$$

$$\mathbb{U}_r = \left\{ v \in \mathbb{H}^1(\Gamma_r) \right\}, \tag{25}$$

where $\mathbb{H}^1$ denotes the Sobolev space on either the concrete domain Ω_c or the reinforcement domain Γ_r.

2.5. Weakening effect caused by the yarns

Instead of considering the weakening effect caused by the yarns by only integrating over the concrete domain Ω_c in $\tilde{a}_c \left(\boldsymbol{u}_c; \delta \boldsymbol{u}_c \right)$, the integration is instead performed over the whole domain Ω, hence

$$\tilde{a}_c \left(\boldsymbol{u}_c; \delta \boldsymbol{u}_c \right) \approx a_c \left(\boldsymbol{u}_c; \delta \boldsymbol{u}_c \right) := \int_{\Omega} \zeta(\boldsymbol{x}) \boldsymbol{\sigma}_c \left(\boldsymbol{\varepsilon}[\boldsymbol{u}_c] \right) : \left[\delta \boldsymbol{u}_c \otimes \boldsymbol{\nabla} \right] \ d\Omega. \tag{26}$$

Instead, the weakening effect from the yarns is considered through the factor ζ, defined as

$$\zeta(\boldsymbol{x}) = \begin{cases} 1 & \text{if } x \in \Omega \setminus \Omega_c', \\ \left(1 - \frac{|\Omega_c'|}{|\Omega_r|} \right) & \text{if } x \in \Omega_c', \end{cases} \tag{27}$$

where Ω_c' is a region centered around the yarns, see Fig. 5.

Note that ζ is decreasing if the reduced zone Ω_c' is increasing, and becomes zero if $|\Omega_r| = |\Omega_c'|$.

Moreover, by approximating the concrete displacement on the interface according to

$$\tilde{\boldsymbol{u}}_c \left(\boldsymbol{x} \right) \approx \boldsymbol{u}_c \left(\boldsymbol{x}_r(\boldsymbol{x}) \right) \text{ on } \partial\Omega_{r,\text{lat}}, \tag{28}$$

it is possible to approximate the bond–slip according to

$$\tilde{s}_l(\boldsymbol{x}) \approx s(\boldsymbol{x}_r) = u_r(\boldsymbol{x}_r) - u_{c,l}(\boldsymbol{x}_r) \text{ on } \Gamma_r. \tag{29}$$

The approximation of the bond–slip in Eq. (29) can now be used to approximate the bond-force T_b according to

$$T_b(\tilde{s}_l) \approx S_r t_{b,l}(s) := S_r \tau_b(s), \tag{30}$$

where $S_r = |\partial A_r|$ is the circumference of the yarn. Note that the bond stress $\tau_b(s)$ is generally a non-linear function of s, as will be specified in Section 5. Eq. (30) can now be used to approximate the coupling form $\tilde{b}(u; \delta v)$ as

$$\tilde{b}(u; \delta v) \approx b(u; \delta v) := S_r \int_{\Gamma_r} \tau_b(u) \ \delta v \ d\Gamma \tag{31}$$

Finally the compatibility condition in Eq. (8) also has to be updated in accordance to Eq. (28), such that

$$\boldsymbol{u}_{r,\perp}(\boldsymbol{x}_r) = \boldsymbol{u}_{c,\perp}(\boldsymbol{x}_r) \text{ on } \Gamma_r. \tag{32}$$

Remark. The approximation in Eq. (31) means that the strong form of the yarn equilibrium can be written as

$$-\frac{dN_r}{dl} + S_r \tau_b = 0 \text{ in } \Gamma_r, \tag{33}$$

$$N_r = 0 \text{ on } \partial\Gamma_r.$$

For consistency, the reduction factor ζ is also applied to the fracture energy G_F and the tensile strength of the concrete $f_{c,t}$ as in Sciegaj et al. (2023). To summarize, the following effective parameters have been used inside Ω_c'

$$E_c' = \zeta E_c \tag{34a}$$

$$G_F' = \zeta G_F \tag{34b}$$

$$f_{c,t}' = \zeta f_{c,t} \tag{34c}$$

3. Upscaling using VCH

To capture the effects stemming from the sub-scale composition of TRC, a two-scale modeling framework is employed. The finer scale, in this work referred to as the sub-scale, is the length scale corresponding to the characteristic length scale of the yarns. The coarse scale, on the other hand, in this work referred to as the large-scale, is the scale at which the structure is modeled, e.g. the plate or shell. To this end, a Representative Volume Element (RVE) at the resolved sub-scale is considered. According to the theory of homogenization, the effective response in a point on the coarser scale can be obtained by averaging the response of this RVE. Formally then, the RVE is defined as the smallest possible unit cell for which the effective response converges (Yvonnet, 2019).

The damage modeling is carried out at the sub-scale; therefore individual cracks are not explicitly depicted at the large scale. The effect of cracking on the constitutive behavior on the large scale is however captured in an average sense in the homogenization, since the effective strain is affected by sub-scale strain localization. It should be noted that it is always possible to go back to the sub-scale and analyze the crack widths etc. in individual RVEs.

Following the approach in Sciegaj et al. (2020), the first step is to additively decompose the sub-scale displacement fields $\boldsymbol{u}_c$ and u_r into a prolonged large-scale part and a fluctuating sub-scale part, such that

$$\boldsymbol{u}_c = \boldsymbol{u}_c^L + \boldsymbol{u}_c^s, \tag{35a}$$

$$u_r = u_r^L + u_r^s, \tag{35b}$$

where the superscripts L and s denotes the large-scale and sub-scale parts respectively. Here u_r^L is chosen as the projection of the large-scale part of the displacement field of the concrete, i.e. $u_r^L = \boldsymbol{e}_l \cdot \boldsymbol{u}_c^L$. The sub-scale displacement fields associated with the concrete and the reinforcement as well as the displacement field on the large scale are illustrated in Fig. 6. On the large scale, the total displacement $\bar{\boldsymbol{u}}$ is decomposed into the mid-plane ($z = 0$) in-plane displacement vector $\bar{\boldsymbol{u}}_p$ and out-of-plane displacement component $\bar{w}$, such that $[\bar{\boldsymbol{u}}] = [\bar{\boldsymbol{u}}_p, \bar{w}]^T$. The in-plane displacements vary linearly through the thickness $z \in [-t/2, t/2]$ of the plate, according to the Kirchhoff–Love plate kinematics

$$\boldsymbol{u}_p^{KL} \left(\bar{\boldsymbol{x}}_p, z \right) = \bar{\boldsymbol{u}}_p - z \boldsymbol{\nabla}_p \bar{w} \big|_{\bar{\boldsymbol{x}}_p}, \tag{36a}$$

$$w^{KL} \left(\bar{\boldsymbol{x}}_p \right) = \bar{w}_{\bar{\boldsymbol{x}}_p}, \tag{36b}$$

where $\boldsymbol{\nabla}_p$ is the in-plane gradient operator.

3.1. Homogenization of sub-scale fields

Following the approach in Börjesson et al. (2023), the upscaling from the sub-scale fields $\boldsymbol{u}_{c,p}$ and w_c to the large-scale fields $\bar{\boldsymbol{u}}_p$, $\bar{h}$, $\bar{w}$, $\bar{\kappa}$ and $\bar{\theta}$ is defined by the homogenization mapping

$$\mathcal{A}^* : \left\{ \boldsymbol{u}_{c,p}, w_c, u_r \right\} \rightarrow \left\{ \bar{\boldsymbol{u}}_\square[\boldsymbol{u}_{c,p}], \bar{h}_\square[\boldsymbol{u}_{c,p}], \bar{w}_\square[\boldsymbol{u}_{c,p}], \bar{\theta}_\square[\boldsymbol{u}_{c,p}], \bar{\kappa}_\square[\boldsymbol{u}_{c,p}] \right\}, \tag{37}$$
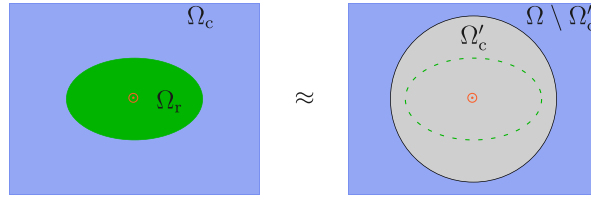
Fig. 5. Reduction zone Ω'_c due to weakening effect from the yarn Ω_r.

where the homogenization operators are defined as

$$\bar{u}_\square[\boldsymbol{u}_{c,p}] := \frac{1}{\left|\Omega_\square\right|} \int_{\Omega_\square} \boldsymbol{u}_{c,p}\ \mathrm{d}\Omega, \tag{38}$$

$$\bar{h}_\square[\boldsymbol{u}_{c,p}] := \frac{1}{\left|\Omega_\square\right|} \int_{\Omega_\square} \left[\boldsymbol{u}_{c,p} \otimes \boldsymbol{\nabla}_p\right]\ \mathrm{d}\Omega, \tag{39}$$

$$\bar{w}_\square[\boldsymbol{u}_{c,p}, w_c] := \frac{1}{\left|\Omega_\square\right|} \int_{\Omega_\square} w_c\ \mathrm{d}\Omega$$
$$- \frac{1}{2\left|\Omega_\square\right|} \int_{\Omega_\square} \left[\boldsymbol{x}_p - \bar{\boldsymbol{x}}_p\right] \cdot \left[\frac{1}{I_\square} \int_{\Omega_\square} z \left[\boldsymbol{u}_{c,p} \otimes \boldsymbol{\nabla}_p\right]^{\mathrm{sym}}\ \mathrm{d}\Omega\right] \cdot \left[\boldsymbol{x}_p - \bar{\boldsymbol{x}}_p\right]\ \mathrm{d}\Omega, \tag{40}$$

$$\bar{\theta}_\square[\boldsymbol{u}_{c,p}] := -\frac{1}{I_\square} \int_{\Omega_\square} z \boldsymbol{u}_{c,p}\ \mathrm{d}\Omega, \tag{41}$$

$$\bar{\kappa}_\square[\boldsymbol{u}_{c,p}] := -\frac{1}{I_\square} \int_{\Omega_\square} z \left[\boldsymbol{u}_{c,p} \otimes \boldsymbol{\nabla}_p\right]^{\mathrm{sym}}\ \mathrm{d}\Omega, \tag{42}$$

where $\left|A_\square\right|$ is the mid-plane area of the RVE and $L_{\square,z}$ is the thickness of the RVE (same thickness as the plate). Note that the choice of homogenization operators means that the homogenization is only done for the concrete displacement fields. $I_\square$ is defined as

$$I_\square = \int_{\Omega_\square} z^2\ \mathrm{d}\Omega = |A| \int_{-L_{\square,z}/2}^{L_{\square,z}/2} z^2\ \mathrm{d}z = \frac{L_{\square,z}^3 \left|A_\square\right|}{12} \tag{43}$$

The second-order prolongation of the vertical displacement results in a coupling between the in-plane and the vertical displacements, necessitating the second term in Eq. (40).

3.2. Prolongation of large-scale fields

The prolongation from the large-scale fields to the large-scale part of the sub–scale fields is defined by the prolongation mapping

$$\mathcal{A} : \left\{\bar{\boldsymbol{u}}_p, \bar{\boldsymbol{h}}, \bar{w}, \bar{\boldsymbol{\theta}}, \bar{\boldsymbol{\kappa}}\right\} \rightarrow \left\{\boldsymbol{u}_{c,p}^L, w_c^L, u_r^L\right\}. \tag{44}$$

The prolongation of the large-scale in-plane displacement field is done using first-order homogenization, i.e. by a first-order Taylor series expansion of Eq. (36a)

$$\boldsymbol{u}_{c,p}^L = \bar{\boldsymbol{u}}_p\left(\bar{\boldsymbol{x}}_p\right) - z\bar{\boldsymbol{\theta}}\left(\bar{\boldsymbol{x}}_p\right) + \bar{\boldsymbol{h}}(\bar{\boldsymbol{x}}_p) \cdot \left[\boldsymbol{x}_p - \bar{\boldsymbol{x}}_p\right] - z\bar{\boldsymbol{\kappa}}\left(\bar{\boldsymbol{x}}_p\right) \cdot \left[\boldsymbol{x}_p - \bar{\boldsymbol{x}}_p\right], \tag{45}$$

where we have introduced the in-plane displacement gradient, curvature tensor and out-of-plane displacement gradient according to

$$\bar{\boldsymbol{h}}(\bar{\boldsymbol{x}}_p) := \left[\bar{\boldsymbol{u}}_p \otimes \boldsymbol{\nabla}_p\right]_{\bar{\boldsymbol{x}}_p}, \tag{46a}$$

$$\bar{\boldsymbol{\kappa}}(\bar{\boldsymbol{x}}_p) := \left[\boldsymbol{\nabla}_p \bar{w} \otimes \boldsymbol{\nabla}_p\right]_{\bar{\boldsymbol{x}}_p}, \tag{46b}$$

$$\bar{\boldsymbol{\theta}}(\bar{\boldsymbol{x}}_p) := \left.\boldsymbol{\nabla}_p \bar{w}\right|_{\bar{\boldsymbol{x}}_p}. \tag{46c}$$

$\bar{\boldsymbol{x}}_p$ is a reference point within the RVE, in this case chosen as the centroid of the RVE. The vertical displacement field $\bar{w}\left(\bar{\boldsymbol{x}}_p\right)$ on the other hand, is prolonged using a second-order Taylor expansion of Eq. (36b), whereby

$$w_c^L = \bar{w}\left(\bar{\boldsymbol{x}}_p\right) + \bar{\boldsymbol{\theta}}\left(\bar{\boldsymbol{x}}_p\right) \cdot \left[\boldsymbol{x}_p - \bar{\boldsymbol{x}}_p\right] + \frac{1}{2}\left[\boldsymbol{x}_p - \bar{\boldsymbol{x}}_p\right] \cdot \bar{\boldsymbol{\kappa}}\left(\bar{\boldsymbol{x}}_p\right) \cdot \left[\boldsymbol{x}_p - \bar{\boldsymbol{x}}_p\right]. \tag{47}$$

The motivation for using a second-order expansion for w_c^L is that we then obtain that the strains are only caused by uniform in-plane and bending deformation and no shear deformations, i.e. that $\boldsymbol{\varepsilon}\left[\boldsymbol{u}_{c,p}^L + w_c^L \boldsymbol{e}_z\right] = \bar{\boldsymbol{h}}^{\mathrm{sym}} - z\bar{\boldsymbol{\kappa}}$. This is fulfilled for the current choice of w_c^L, see Eq. (C.3).

Remark. First-order prolongation of the vertical part of the displacement field w_c^L would result in an extra shear strain term $-\frac{1}{2}\bar{\boldsymbol{\kappa}}\cdot\left[\boldsymbol{x}_p - \bar{\boldsymbol{x}}_p\right]\otimes \boldsymbol{e}_z$ in the expression for the strain tensor.

The next step is to approximate the integrals of the fully resolved weak form by integrating the running averages over the sub-domains $\Omega_\square = A_\square \times \left[-L_{\square,z}/2, L_{\square,z}/2\right]$, the RVEs. Consequently, for any functions f and g defined on Ω and Γ_r respectively, the following approximation is done

$$\int_\Omega f\ \mathrm{d}\Omega + \int_{\Gamma_r} g\ \mathrm{d}\Gamma \approx \int_A \langle f \rangle + \langle\langle g \rangle\rangle\ \mathrm{d}A, \tag{48}$$

where $\langle f \rangle$ and $\langle\langle g \rangle\rangle$ are the homogenization operators on $\Omega_\square$ and $\Gamma_{\square,r}$ respectively, defined as

$$\langle f \rangle = \frac{1}{\left|A_\square\right|} \int_{\Omega_\square} f\ \mathrm{d}\Omega, \tag{49}$$

$$\langle\langle g \rangle\rangle = \frac{1}{\left|A_\square\right|} \int_{\Gamma_{\square,r}} g\ \mathrm{d}\Gamma. \tag{50}$$

Inserting the approximation in Eq. (48) into the weak form of the fully resolved problem in Eq. (18) yields

$$\int_A a_{\square,c}\left(\boldsymbol{u}_c; \delta\boldsymbol{u}_c\right) + b_\square\left(s; \delta u_r - \boldsymbol{e}_1 \cdot \delta\boldsymbol{u}_c\right)$$
$$+ a_{\square,r}\left(u_r; \delta u_r\right)\ \mathrm{d}A = l_c\left(\delta\boldsymbol{u}_c\right), \quad \forall \delta\boldsymbol{u}_c \in \mathbb{U}_c^0, \quad \forall \delta u_r \in \mathbb{U}_r. \tag{51}$$

Note that both the body forces $\hat{\boldsymbol{b}}$ and the boundary tractions $\hat{\boldsymbol{t}}$ are assumed to be smooth on the sub-scale, hence $\left\langle \hat{\boldsymbol{b}} \cdot \delta\boldsymbol{u}_c \right\rangle \approx \hat{\boldsymbol{b}} \cdot \delta\boldsymbol{u}_c$ and $\left\langle \hat{\boldsymbol{t}} \cdot \delta\boldsymbol{u}_c \right\rangle \approx \hat{\boldsymbol{t}} \cdot \delta\boldsymbol{u}_c$. Also, note that the integration is now performed over the averaged forms in Eqs. (26), (20) and (31), such as

$$a_{\square,c}\left(\boldsymbol{u}_c; \delta\boldsymbol{u}_c\right) := \frac{1}{\left|A_\square\right|} \int_{\Omega_\square} \zeta(\boldsymbol{x})\sigma_c\left(\boldsymbol{\varepsilon}[\boldsymbol{u}_c]\right) : \left[\delta\boldsymbol{u}_c \otimes \boldsymbol{\nabla}\right]\ \mathrm{d}\Omega, \tag{52}$$

$$a_{\square,r}\left(u_r; \delta u_r\right) := \frac{1}{\left|A_\square\right|} \int_{\Gamma_{r,\square}} N_r\left(\frac{du_r}{dl}\right) \frac{d\delta u_r}{dl}\ \mathrm{d}\Gamma, \tag{53}$$

$$b_\square(u; \delta v) := \frac{1}{\left|A_\square\right|} \int_{\Gamma_{r,\square}} S_r \tau_b(u)\delta v\ \mathrm{d}\Gamma. \tag{54}$$

3.3. Compatibility between homogenization and prolongation

To ensure a proper unique mapping, we require that the homogenized sub-scale fields should be zero, i.e that

$$\mathcal{A}^* : \left\{\boldsymbol{u}_{c,p}^s, w_c^s, u_r^s\right\} = \{0, 0, 0, 0, 0\} \tag{55}$$

Consequently, for compatibility reasons, the homogenized large-scale parts of the fields must equal the large-scale fields, i.e. that

$$\mathcal{A}\left(\hat{\bar{\boldsymbol{u}}}_p, \hat{\bar{\boldsymbol{h}}}, \hat{\bar{w}}, \hat{\bar{\boldsymbol{\kappa}}}, \hat{\bar{\boldsymbol{\theta}}}\right) = \left\{\hat{\boldsymbol{u}}_{c,p}^L, \hat{w}_c^L, \hat{u}_r^L\right\}, \tag{56a}$$

$$\mathcal{A}^*\left(\hat{\boldsymbol{u}}_{c,p}^L, \hat{w}_c^L, \hat{u}_r^L\right) = \left\{\hat{\bar{\boldsymbol{u}}}_p, \hat{\bar{\boldsymbol{h}}}, \hat{\bar{w}}, \hat{\bar{\boldsymbol{\kappa}}}, \hat{\bar{\boldsymbol{\theta}}}\right\}, \tag{56b}$$
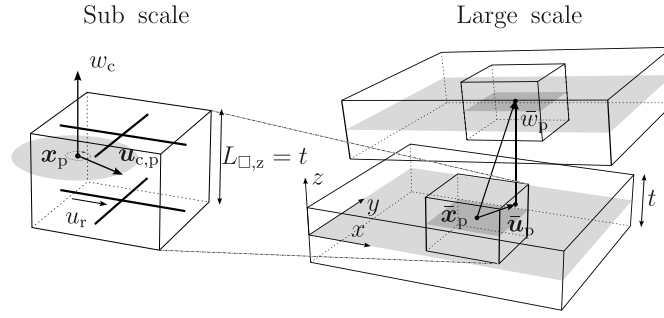
Fig. 6. Displacement fields on the sub-scale and the large-scale. Note that the height of the RVE $L_{\square,z}$ is the same as the plate thickness t, hence homogenization is only performed in the plane of the plate.

for any choice of $\left\{ \hat{\bar{u}}_\mathrm{p}, \hat{\bar{h}}, \hat{\bar{w}}, \hat{\bar{\kappa}}, \hat{\bar{\theta}} \right\}$. The fulfillment of Eq. (56) is shown in Appendix A.1.

3.4. Large-scale problem

The large-scale plate problem is derived from Eq. (51) by testing with the prolonged large-scale displacements $\delta \boldsymbol{u}_\mathrm{c}^\mathrm{L}$ (Sciegaj et al., 2020).

$$\int_A \frac{1}{|A_\square|} \left(\int_{\Omega_\square} \boldsymbol{\sigma}_\mathrm{c} \left(\boldsymbol{\varepsilon}[\boldsymbol{u}_\mathrm{c}] \right) : \left[\delta \boldsymbol{u}_\mathrm{c}^\mathrm{L} \otimes \boldsymbol{\nabla} \right] \mathrm{d}\Omega + \int_{\Gamma_{\mathrm{r},\square}} N_\mathrm{r} \frac{\partial \delta u_\mathrm{r}^\mathrm{L}}{\partial l} \mathrm{d}\Gamma \right) \mathrm{d}A$$
$$= \int_{\partial A} \hat{\boldsymbol{t}} \cdot \delta \boldsymbol{u}_\mathrm{c}^\mathrm{L} \, \mathrm{d}\Gamma + \int_A \hat{\boldsymbol{b}} \cdot \delta \boldsymbol{u}_\mathrm{c}^\mathrm{L} \, \mathrm{d}A. \tag{57}$$

Note that the coupling term disappears since we are testing with the large-scale displacements, hence $\delta u_\mathrm{r}^\mathrm{L} - \boldsymbol{e}_1 \cdot \delta \boldsymbol{u}_\mathrm{c}^\mathrm{L} = \boldsymbol{e}_1 \cdot \delta \boldsymbol{u}_\mathrm{c}^\mathrm{L} - \boldsymbol{e}_1 \cdot \delta \boldsymbol{u}_\mathrm{c}^\mathrm{L} = 0$.

The first term in Eq. (57) can be evaluated using the expression for the gradient of the large-scale part of the concrete displacement in Eq. (C.5)

$$\int_{\Omega_\square} \boldsymbol{\sigma}_\mathrm{c} : \left[\delta \boldsymbol{u}_\mathrm{c}^\mathrm{L} \otimes \boldsymbol{\nabla} \right] \mathrm{d}\Omega = \int_{\Omega_\square} \boldsymbol{\sigma}_{\mathrm{c},\mathrm{p}} : \bar{\boldsymbol{h}}[\delta \bar{\boldsymbol{u}}_\mathrm{p}] - z\boldsymbol{\sigma}_{\mathrm{c},\mathrm{p}} : \bar{\boldsymbol{\kappa}}[\delta \bar{w}] \, \mathrm{d}\Omega, \tag{58}$$

where the symmetry of the stress tensor $\boldsymbol{\sigma}_\mathrm{s}$ was used so that all terms related to the anti-symmetric part of $\left[\delta \boldsymbol{u}_\mathrm{c}^\mathrm{L} \otimes \boldsymbol{\nabla} \right]$ vanish. Left are the terms involving the in-plane components of the stress tensor $\boldsymbol{\sigma}_{\mathrm{c},\mathrm{p}}$

$$[\boldsymbol{\sigma}_{\mathrm{c},\mathrm{p}}] = \begin{bmatrix} \sigma_{xx} & \sigma_{xy} \\ \sigma_{yx} & \sigma_{yy} \end{bmatrix}.$$

The second term involves the derivative of the large-scale yarn displacement and can be evaluated as

$$\int_{\Gamma_{\mathrm{r},\square}} N_\mathrm{r} \frac{\mathrm{d}\delta u_\mathrm{r}^\mathrm{L}}{\mathrm{d}l} \mathrm{d}\Gamma = \int_{\Gamma_{\mathrm{r},\square}} N_\mathrm{r} \boldsymbol{e}_1 \otimes \boldsymbol{e}_1 : \bar{\boldsymbol{h}}[\delta \bar{\boldsymbol{u}}_\mathrm{p}] - N_\mathrm{r} z \boldsymbol{e}_1 \otimes \boldsymbol{e}_1 : \bar{\boldsymbol{\kappa}}[\delta \bar{\boldsymbol{u}}_\mathrm{p}] \, \mathrm{d}\Gamma, \tag{59}$$

where the derivative of u_r^L is evaluated in Appendix C.1.

Finally, by inserting Eqs. (58) and (59) in Eq. (57), the LHS can be expanded as

$$\int_A \left(\bar{\boldsymbol{h}}[\delta \bar{\boldsymbol{u}}_\mathrm{p}] : \frac{1}{|A_\square|} \left[\int_{\Omega_\square} \boldsymbol{\sigma}_{\mathrm{c},\mathrm{p}} \, \mathrm{d}\Omega + \int_{\Gamma_{\mathrm{r},\square}} N_\mathrm{r} \boldsymbol{e}_1 \otimes \boldsymbol{e}_1 \, \mathrm{d}\Gamma \right] \right.$$
$$\left. - \bar{\boldsymbol{\kappa}}[\delta \bar{w}] : \frac{1}{|A_\square|} \left[\int_{\Omega_\square} z\boldsymbol{\sigma}_{\mathrm{c},\mathrm{p}} \, \mathrm{d}\Omega + \int_{\Gamma_{\mathrm{r},\square}} N_\mathrm{r} z \boldsymbol{e}_1 \otimes \boldsymbol{e}_1 \, \mathrm{d}\Gamma \right] \right) \mathrm{d}A. \tag{60}$$

From this, the effective membrane forces and bending moments can be identified as

$$\bar{\boldsymbol{N}} = \frac{1}{|A_\square|} \left[\int_{\Omega_\square} \boldsymbol{\sigma}_{\mathrm{c},\mathrm{p}} \, \mathrm{d}\Omega + \int_{\Gamma_{\mathrm{r},\square}} N_\mathrm{r} \boldsymbol{e}_1 \otimes \boldsymbol{e}_1 \, \mathrm{d}\Gamma \right], \tag{61}$$

$$\bar{\boldsymbol{M}} = -\frac{1}{|A_\square|} \left[\int_{\Omega_\square} z\boldsymbol{\sigma}_{\mathrm{c},\mathrm{p}} \, \mathrm{d}\Omega + \int_{\Gamma_{\mathrm{r},\square}} N_\mathrm{r} z \boldsymbol{e}_1 \otimes \boldsymbol{e}_1 \, \mathrm{d}\Gamma \right]. \tag{62}$$

Remark. It can be proven that the effective membrane forces and moments are only dependent on the large-scale in-plane strains, i.e. that $\bar{\boldsymbol{N}} = \bar{\boldsymbol{N}}\{\bar{\varepsilon}, \bar{\kappa}\}$ and curvatures $\bar{\boldsymbol{M}} = \bar{\boldsymbol{M}}\{\bar{\varepsilon}, \bar{\kappa}\}$, see Appendix D. This means that both the membrane forces and moments are invariant under rigid body motion $\bar{\boldsymbol{u}}_\mathrm{p}$, $\bar{w}$ and $\bar{\theta}$.

Finally, by using the definitions of $\bar{\boldsymbol{N}}$ and $\bar{\boldsymbol{M}}$, the large-scale problem in Eq. (57) can be written as

$$\int_A \bar{\boldsymbol{h}}(\delta \bar{\boldsymbol{u}}_\mathrm{p}) : \bar{\boldsymbol{N}} + \bar{\boldsymbol{\kappa}}(\delta \bar{w}) : \bar{\boldsymbol{M}} \mathrm{d}A = l\left(\delta \bar{\boldsymbol{u}}_\mathrm{p}, \delta \bar{w} \right), \forall \delta \bar{\boldsymbol{u}}_\mathrm{p} \in \bar{\mathbb{U}}^0, \forall \delta \bar{w} \in \bar{\mathbb{W}}^0, \tag{63}$$

where the loading form $l\left(\delta \bar{\boldsymbol{u}}_\mathrm{p}, \delta \bar{w} \right)$ can be evaluated in terms of the large-scale displacement fields by substituting Eqs. (45) and (47) for $\delta \boldsymbol{u}_\mathrm{c}^\mathrm{L}$ in Eq. (57). The membrane forces and moments tensors can be expressed in terms of the Cartesian components

$$[\bar{\boldsymbol{N}}] = \begin{bmatrix} \bar{N}_{xx} & \bar{N}_{xy} \\ \bar{N}_{yx} & \bar{N}_{yy} \end{bmatrix}, [\bar{\boldsymbol{M}}] = \begin{bmatrix} \bar{M}_{xx} & \bar{M}_{xy} \\ \bar{M}_{yx} & \bar{M}_{yy} \end{bmatrix},$$

where the first index denotes the normal of the section and the second index denotes the direction of the associated stress, see Fig. 7. Note that both tensors are symmetric, i.e. that $\bar{\boldsymbol{N}} = \bar{\boldsymbol{N}}^\mathrm{T}$ and $\bar{\boldsymbol{M}} = \bar{\boldsymbol{M}}^\mathrm{T}$.

3.5. Sub-scale problem

If the fully resolved problem in Eq. (51) is instead localized on the RVE and tested with sub-scale displacement test functions, the sub-scale problem can be derived (Sciegaj et al., 2020). The weak form of the sub-scale problem, before specifying the boundary conditions, can be formulated as: Find $\boldsymbol{u}_\mathrm{c}^\mathrm{s} \in \mathbb{U}_{\square,\mathrm{c}}$ and $u_\mathrm{r}^\mathrm{s} \in \mathbb{U}_{\square,\mathrm{r}}$ such that

$$a_{\square,\mathrm{c}} \left(\boldsymbol{u}_\mathrm{c}^\mathrm{L} + \boldsymbol{u}_\mathrm{c}^\mathrm{s}; \delta \boldsymbol{u}_\mathrm{c} \right) - b_\square \left(u_\mathrm{r}^\mathrm{s} - \boldsymbol{e}_1 \cdot \boldsymbol{u}_\mathrm{c}^\mathrm{s}; \boldsymbol{e}_1 \cdot \delta \boldsymbol{u}_\mathrm{c}^\mathrm{s} \right) = 0 \quad \forall \delta \boldsymbol{u}_\mathrm{c}^\mathrm{s} \in \mathbb{U}_{\square,\mathrm{c}}, \tag{64a}$$

$$a_{\square,\mathrm{r}} \left(u_\mathrm{r}^\mathrm{L} + u_\mathrm{r}^\mathrm{s}; \delta u_\mathrm{r}^\mathrm{s} \right) + b_\square \left(u_\mathrm{r}^\mathrm{s} - \boldsymbol{e}_1 \cdot \boldsymbol{u}_\mathrm{c}^\mathrm{s}; \delta u_\mathrm{r}^\mathrm{s} \right) = 0 \quad \forall \delta u_\mathrm{r}^\mathrm{s} \in \mathbb{U}_{\square,\mathrm{r}}, \tag{64b}$$

with suitable trial/test spaces, which will be specified for each of the boundary conditions in Section 3.6.

Note that the weak form is formulated in terms of the sought-for sub-scale displacements $\boldsymbol{u}_\mathrm{c}^\mathrm{s}$ and u_r^s instead of the total displacements $\boldsymbol{u}_\mathrm{c}$ and u_r as in Eq. (51). Also, note that there is no large-scale contribution to $b_\square(u; \delta v)$ since $u_\mathrm{r}^\mathrm{L} = \boldsymbol{e}_1 \cdot \boldsymbol{u}_\mathrm{c}^\mathrm{L}$.

3.6. Boundary conditions on the RVE

It is necessary to prescribe boundary conditions on the RVE to obtain a solvable system. In this study, three different types of boundary conditions are considered. An upper bound of the response is obtained by prescribing the large-scale displacement field, referred to as Dirichlet boundary condition. An intermediate solution is obtained by applying strongly periodic boundary conditions, i.e. we strongly enforce that the displacements on opposite boundaries are equal. A
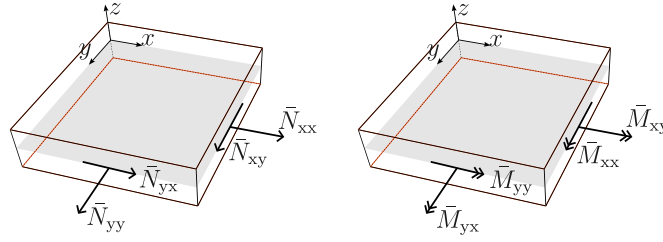
Fig. 7. Convention used for the moment and membrane force vectors, for the Cartesian coordinate system in the figure.
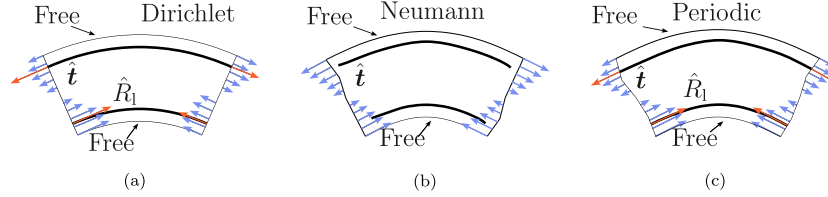

Fig. 8. Illustration of the different boundary conditions for the case of uniaxial bending and membrane strain. (a) Dirichlet boundary conditions. (b) Strongly periodic boundary conditions (c) Neumann boundary conditions.

lower bound, referred to as Neumann conditions, is obtained by using constant large-scale membrane forces and moments to derive the prescribed traction on the vertical faces of the RVE, see Fig. 8.

3.6.1. Dirichlet boundary condition

The sub-scale fluctuations of the displacement field u_c^s are assumed to vanish on the vertical boundaries. This means that

$$u_c = u_c^L \text{ on } \Gamma_\square, \tag{65a}$$

$$u_r = u_r^L \text{ on } \Gamma_{\square,r} \cap \Gamma_\square, \tag{65b}$$

where the large-scale part of the displacement is given by Eqs. (45) and (47). The corresponding trial and test spaces pertinent to the Dirichlet boundary condition are then

$$\mathbb{U}_{\square,c}^{DBC} = \left\{ u \in [\mathbb{H}^1(\Omega_\square)]^3, u = \mathbf{0} \text{ on } \Gamma_\square \right\}, \tag{66a}$$

$$\mathbb{U}_{\square,r}^{DBC} = \left\{ v \in \mathbb{H}^1(\Gamma_{\square,r}), v = 0 \text{ on } \Gamma_{\square,r} \cap \Gamma_\square \right\}. \tag{66b}$$

3.6.2. Strongly periodic boundary condition

Instead of assuming that the fluctuation field u_c^s is zero on the boundary of the RVE as for the Dirichlet condition, we assume that the sub-scale part of the displacement field is periodic on the boundary, i.e. that

$$[\![u_c^s]\!] = 0 \quad \text{on} \quad \Gamma_\square^+, \tag{67}$$

where the jump operator is defined as $[\![u]\!] = u(x) - u(\varphi_{per}(x))$, see Fig. 9.

From Eq. (67) it follows that the total displacement jump must equal the large-scale part of the displacement jump, i.e. that

$$[\![u_c]\!] = [\![u_c^L + u_c^s]\!] = [\![u_c^L]\!] \text{ on } \Gamma_\square^+. \tag{68}$$

By inserting the large-scale part of the displacements from Eqs. (45) and (47) in Eq. (68), we obtain

$$[\![u_{c,p}]\!] = \bar{h}(\bar{x}_p) \cdot [\![x_p]\!] - z\bar{\kappa}(\bar{x}_p) \cdot [\![x_p]\!] \text{ on } \Gamma_\square^+, \tag{69a}$$

$$[\![w_c]\!] = \bar{\theta}(\bar{x}_p) \cdot [\![x_p]\!] + \frac{1}{2}\bar{\kappa}(\bar{x}_p) : [\![x_p \otimes x_p]\!] \text{ on } \Gamma_\square^+. \tag{69b}$$

where $[\![x_p]\!]$ is the length of the RVE in the respective direction. Note that all terms being constant within the RVE vanish and that the terms
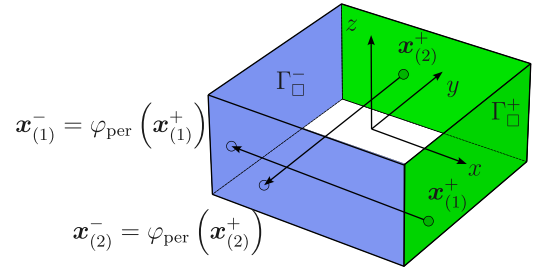

Fig. 9. Mapping between the image and mirror boundaries $\varphi_{per} : \Gamma^+ \mapsto \Gamma^-$ for the RVE.

in Eq. (69b) involving $[\![x_p^2]\!]$ and $[\![y_p^2]\!]$ are zero. The same periodicity constraint is also applied to the reinforcement, i.e.

$$[\![u_r]\!] = e_1 \cdot [\![u_c^L]\!] \text{ on } \Gamma_\square^+, \tag{70}$$

Note that it is possible to move e_1 outside the jump operator since the direction of the yarns is assumed to be constant in the RVE. Further, note that this boundary condition is invariant under translation for both the concrete and the yarns, hence the displacement must be prescribed to prevent rigid body motion. For the concrete, the displacement is prescribed in one of the corners. For the yarns, the displacement at the ends is prescribed to the same value as the concrete displacement at that point. The trial/test spaces pertinent to the strongly periodic boundary condition are then

$$\mathbb{U}_{\square,c}^{SPBC} = \left\{ u \in [\mathbb{H}^1(\Omega_\square)]^3, [\![u]\!] = \mathbf{0} \text{ on } \Gamma_\square^+, \int_{\Omega_\square} u \, d\Omega = \mathbf{0} \right\}, \tag{71a}$$

$$\mathbb{U}_{\square,r}^{SPBC} = \left\{ v \in \mathbb{H}^1(\Gamma_{\square,r}), [\![v]\!] = 0 \text{ on } \Gamma_{\square,r} \cap \Gamma_\square^+ \right\}. \tag{71b}$$

3.6.3. Neumann boundary condition

For the Neumann boundary condition, the prescribed boundary traction on the RVE is assumed to be caused by constant membrane forces $\bar{N} \in \mathbb{R}^{2\times2}$ and bending moments $\bar{M} \in \mathbb{R}^{2\times2}$. These boundary conditions can be imposed either by adding the following weak constraints

$$\delta\bar{M} : \bar{\kappa}_\square[u_c] = \delta\bar{M} : \bar{\kappa}, \tag{72a}$$

$$\delta\bar{N} : \bar{h}_\square[u_c] = \delta\bar{N} : \bar{h}, \tag{72b}$$

where $\bar{N}$ and $\bar{M}$ act as Lagrange multipliers, or by enforcing the strong form of the constraints, i.e. that

$$\bar{\kappa}_\square[u_c] = \bar{\kappa}, \tag{73a}$$

$$\bar{h}_\square[u_c] = \bar{h}. \tag{73b}$$

Note that the constraint in Eqs. (73b) and (73a) only applies to the concrete boundary $\Gamma_\square^+$. Consequently, the reinforcement is free to move at the boundaries $\partial \bar{\Gamma}_r$. In this work, the constraints are implemented using the strong form as in Eqs. (73a) and (73b).

Rigid body translations are constrained by locking the x,y and z displacements in one of the nodes, the z and y displacements in one other and finally the y displacement in three of the nodes in the xy-plane. The trial and test spaces pertinent to the Neumann boundary condition are then

$$\mathbb{U}_{\square,c}^{NBC} = \{u \in [\mathbb{H}^1(\Omega_\square)]^3, \bar{\kappa}_\square[u] = \bar{h}_\square[u] = 0 \text{ in } \Omega_\square, \int_{\Omega_\square} u \, d\Omega = 0\}, \tag{74a}$$

$$\mathbb{U}_{\square,r}^{NBC} = \{v \in \mathbb{H}^1(\Gamma_{\square,r})\}. \tag{74b}$$

Remark. By using the expression for the effective curvature in Eq. (42), together with the Gauss divergence theorem, Eq. (73a) can be expressed in terms of the displacement jump at the boundary

$$\bar{\kappa}_\square[u_c^s] = -\frac{1}{I_\square} \int_{\Gamma_\square^+} \frac{z}{2} n_{\square,j} [\![u_{c,p,i}^s]\!] + \frac{z}{2} n_{\square,i} [\![u_{c,p,j}^s]\!] \, d\Gamma = 0, \tag{75}$$

where $n_\square$ is the unit normal of the RVE boundary. See Appendix B for the derivation. Similarly, Eq. (73b) can be expanded using Eq. (39) such that

$$\bar{h}_\square[u_c^s] = \frac{1}{|\Omega_\square|} \int_{\Gamma_\square^+} [\![u_{c,p}^s]\!] \otimes n_\square \, d\Gamma = 0. \tag{76}$$

4. Numerical implementation

The sub-scale problem, as defined in Eqs. (64a) and (64b) is solved using the finite element software COMSOL. The concrete displacement field is approximated using linear hexahedron elements. The sufficient number of elements used for the FE-mesh for the RVEs is determined by studying the convergence of the linear elastic effective bending moment $\bar{M}_{xx}$ for the 2 × 2 yarn RVE. From this analysis, a mesh consisting of 2000 elements for the concrete and 16 truss elements for each yarn, is deemed sufficient for the RVE consisting of 2 × 2 yarns. The number of elements for the other RVE sizes is then scaled in proportion to the size to maintain the same element resolution. The distance from the center of the yarns to the edge of the concrete is 3.125 mm for all studies. The material models and parameters used for the analysis are described in the following sections.

4.1. Yarns

The constitutive model used for the yarns is shown in Fig. 10. In this model, the yarns are only developing a normal stress in tension. Since the yarns are assumed to exhibit micro-buckling already at a small stress level, they are modeled as stress-free in compression. Additionally, the yarns are assumed to lose all load-carrying capacity once the stress reaches the ultimate stress f_u. The material parameters used for the yarns are sourced from Sciegaj et al. (2022) and correspond to a textile designated StoFRP Grid 1000 C 390 with yarn dimensions 3.55 mm × 0.39 mm , see Table 1. The stiffness reduction factor η_E has been calibrated in Sciegaj et al. (2022) together with the parameters for the bond–slip model, see Section 4.3 for a more comprehensive account of the calibration procedure. In the same work, the efficiency factor for the strength η_f has been calibrated directly by comparing the capacity obtained from tensile tests with the values provided by the manufacturer.
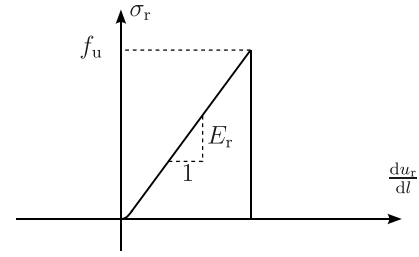

Fig. 10. Constitutive relation used for the yarns.

Table 1
Material properties for the concrete matrix and the yarns.

Parameter	Value	Unit
Tensile strength concrete, $f_{c,t}$	4.35	MPa
Ultimate compressive strain concrete, $\varepsilon_{c,u}$	2.9×10^{-3}	–
Compressive strength concrete, $f_{c,c}$	67.8	MPa
Young's modulus concrete, E_c	40.7	GPa
Poisson's ratio concrete, ν_c	0.2	–
Fracture energy concrete, G_F	156	N m^{-1}
Damage parameter, β	1.06	–
Damage parameter, A_c	2.04	–
Damage parameter, B_c	1.500×10^3	–
Compressive strain threshold, $\varepsilon_{0,c}$	3.39×10^{-4}	–
Nominal young's modulus yarns, $E_{r,0}$	242	GPa
Nominal tensile strength yarns, $f_{u,0}$	3.97	GPa
Efficiency factor tensile strength yarns, η_f	0.34	–
Efficiency factor stiffness yarns, η_E	0.34	–

4.2. Concrete

The material parameters used for the concrete matrix are sourced from Sciegaj et al. (2022) and are gathered in Table 1. Based on the compressive strength, the concrete approximately corresponds to a strength class of C60/75, on which the ultimate strain is based (European Organization for Standardization, 2004).

The parameters used for the damage modeling are presented in Table 1. For regularization, a crack-band width h_{cb} equal to the element length is used, as the elements are cube-shaped. It was later verified that the strain localized in one element row. To trigger strain localization, a uniform variation with a range of 5% is applied to the tensile strength f_u, fracture energy G_f and the Young's modulus E_c in Ω. Moreover, the stiffness reduction factor ζ, accounting for the weakening effect of the yarns, is calculated from Eq. (27) for a region $|\Omega_c'| = 2.76 \text{ mm}^2$ centered around the yarns, yielding $\zeta = 0.51$ in Ω_c'.

4.3. Bond–slip model

The bond slip-stress model $\tau_b(s)$ adopted in this work has been developed by Sciegaj et al. in Sciegaj et al. (2022), and is based on a bond–slip relation from Model Code 2010, see Fig. 11.

The parameters that control the bond slip-stress curve are τ_{max}, τ_f, s_0, s_1, s_2, s_3, α. These parameters have been calibrated in Sciegaj et al. (2022) by using an optimization scheme minimizing the overall discrepancy in the crack opening-force relation between numerical and experimental results from a pull-out experiment. The values used for these parameters are presented in Table 2. Note that these values are valid for the specific combination of textile and concrete used, see 4.1 and 4.2. To account for degradation and subsequent unloading and reloading, a linear branch is added in this work. During loading, the bond stress evolution follows the virgin curve $\tau_{b,v}$ in Fig. 11 and during unloading/reloading the bond stress evolution follows the linear branch.
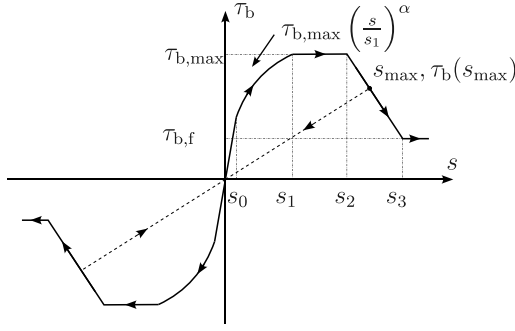
Fig. 11. Bond slip-stress relation employed in the analysis.

Table 2
Bond–slip model parameters.

Parameter	Value	Unit
τ_{f}	0.822	MPa
τ_{max}	2.910	MPa
α	0.316	–
s_0	0.015	mm
s_1	0.025	mm
s_2	0.086	mm
s_3	1.092	mm

5. Numerical studies

Numerical studies are performed to validate the model and to demonstrate its capabilities for some applications. In Section 5.1, the influence of RVE-size and boundary conditions is investigated. Particularly, the convergence properties of the stiffness tensors are investigated. The upscaling framework is then validated against an analytical solution for the case of uniaxial bending in Section 5.2. Finally, in Section 5.3, the model is validated against fully resolved one-way and two-way slabs, both when the membrane displacements are prescribed (Sections 5.3.1 and 5.3.2) and when membrane tractions are prescribed (Section 5.3.3). Material models and parameters used in the simulations are presented in Section 4.

5.1. Influence of boundary conditions and RVE size

The effect of increasing the RVE-size is analyzed by studying the eigenvalues of the linear membrane and bending stiffness tensors. In the linear regime, it is possible to directly relate the membrane forces and the in-plane strains and curvatures using the membrane stiffness $\bar{\boldsymbol{D}}^{\text{M}}$ and the coupling stiffness $\bar{\boldsymbol{D}}^{\text{M,B}}$ as well as the curvatures and strains and the bending moments using the bending stiffness tensor $\bar{\boldsymbol{D}}^{\text{B}}$ and the coupling stiffness $\bar{\boldsymbol{D}}^{\text{B,M}}$

$$\bar{\boldsymbol{N}} = \bar{\boldsymbol{D}}^{\text{M}} : \bar{\boldsymbol{\varepsilon}} + \bar{\boldsymbol{D}}^{\text{M,B}} : \bar{\boldsymbol{\kappa}}, \tag{77a}$$

$$\bar{\boldsymbol{M}} = \bar{\boldsymbol{D}}^{\text{B,M}} : \bar{\boldsymbol{\varepsilon}} + \bar{\boldsymbol{D}}^{\text{B}} : \bar{\boldsymbol{\kappa}}, \tag{77b}$$

where the coupling terms arise since the coordinate system is fixed at the mid-plane of the plate and to account for a non-symmetric stiffness about the mid-plane. Using the symmetry of $\bar{\boldsymbol{N}}$, $\bar{\boldsymbol{M}}$, $\bar{\boldsymbol{\varepsilon}}$ and $\bar{\boldsymbol{\kappa}}$, the in-plane strains and the curvatures can be written using Voigt notation as $\underline{\bar{\varepsilon}} = \begin{bmatrix} \bar{\varepsilon}_{\text{xx}} & \bar{\varepsilon}_{\text{yy}} & 2\bar{\varepsilon}_{\text{xy}} \end{bmatrix}^{\text{T}}$, $\underline{\bar{\kappa}} = \begin{bmatrix} \bar{\kappa}_{\text{xx}} & \bar{\kappa}_{\text{yy}} & 2\bar{\kappa}_{\text{xy}} \end{bmatrix}^{\text{T}}$. Consequently, the Cartesian components of the membrane stiffness tensor are obtained by subjecting the RVE to unit strain perturbations $\hat{\varepsilon}_{\text{xx}}, \hat{\varepsilon}_{\text{yy}}$ and $\hat{\varepsilon}_{\text{xy}}$. Similarly, for the bending stiffness tensor, the components are obtained by subjecting the RVE to unit curvature perturbations $\hat{\kappa}_{\text{xx}}, \hat{\kappa}_{\text{yy}}$ and $\hat{\kappa}_{\text{xy}}$.

An analysis using four different RVE sizes and the three different boundary conditions described in Section 3.6 is performed to study the effect of increasing the RVE size. The two smallest of the four RVEs,
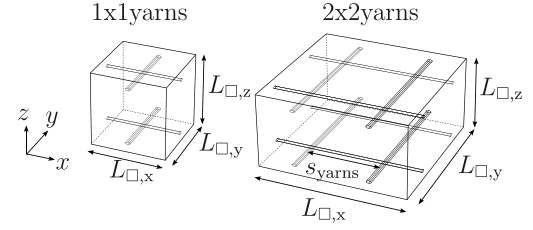
Fig. 12. Geometry of the 1×1 and 2×2 yarn RVEs.

ranging in size from 1×1 to 8×8 yarns, are illustrated in Fig. 12. The spacing between the yarns s_{yarns} and the plate thickness $L_{\square,\text{z}}$ is 15 mm for all four sizes. The results, in terms of the largest eigenvalues of the respective stiffness tensor $\bar{\boldsymbol{D}}^{\text{M}}$ and $\bar{\boldsymbol{D}}^{\text{B}}$, are displayed in Fig. 13. Starting with the membrane stiffness in Fig. 13(a), it is evident that the Neumann and Dirichlet boundary conditions provide lower and upper bounds on the stiffness, just as expected since the influence from the boundary conditions decreases when the RVE size increases. Looking at the same graphs, one can also observe that the stiffness is converging for an increasing RVE size, with a faster convergence rate for the Dirichlet boundary condition. The same convergence behavior can also be observed for the bending stiffness, see Fig. 13(b). There is, however, a slightly larger relative difference between the periodic and Neumann boundary conditions.

5.2. Validation against analytical solution

To validate the proposed upscaling framework, the results obtained for the case of uniaxial bending are compared to results obtained from a simplified analytical beam model. In the linear regime (stage I), the response is fully determined by the concrete stiffness. In the post-cracking regime, the concrete stress is obtained from the curvature using Eq. (5).6 in European Organization for Standardization (2004). Eq. 9.28 in European Organization for Standardization (2004) is used to interpolate the moment in the tension stiffening regime, i.e. in the region immediately after cracking has occurred. Furthermore, full interaction is assumed between the yarns and the concrete, and the RVE is assumed to be fully cracked. The former assumption contributes to an overestimation of the bending moment while the latter assumption contributes to an underestimation of the bending moment. The comparison with the analytical solution is performed for a RVE subjected to pure uniaxial bending, i.e. $\bar{M}_{\text{xx}} \neq 0$ kNm/m while $\bar{N}_{\text{xx}} = 0$ kN/m.

The numerical simulation is performed using displacement control, therefore $\bar{N}_{\text{xx}} = \bar{N}_{\text{yy}} = 0$ kN/m and $\bar{M}_{\text{yy}} = 0$ kNm/m were added as point-wise strong constraints to allow the mid-plane to stretch and the beam to bend in the transverse direction, as assumed in the beam model. The simulation is performed for the three different boundary conditions described in 3.6. The result in terms of effective bending moment is presented in Fig. 14(a).

Looking at the curvature-moment response in Fig. 14(a), one can see that there is a good agreement between the moment from the analytical solution and the RVE model, especially when using the periodic boundary conditions. In particular, cracking occured at approximately the same curvature as in the analytical model for all boundary conditions, approximately 0.02 m^{-1}. Also, the bending stiffness is accurately predicted using the proposed upscaling technique. On the other hand, the analysis using the Neumann boundary condition fails already at a small curvature. This is because the prescribed traction on the boundary locally ruptured the concrete at cracking. Furthermore, as expected, the Dirichlet and Neumann boundary conditions provide upper and upper and lower bounds on the effective bending moment and the periodic boundary conditions provide an intermediate solution. By studying the post-cracking regime in Fig. 14(a), it is evident that the effective curvature-moment response obtained using the upscaling from the RVE
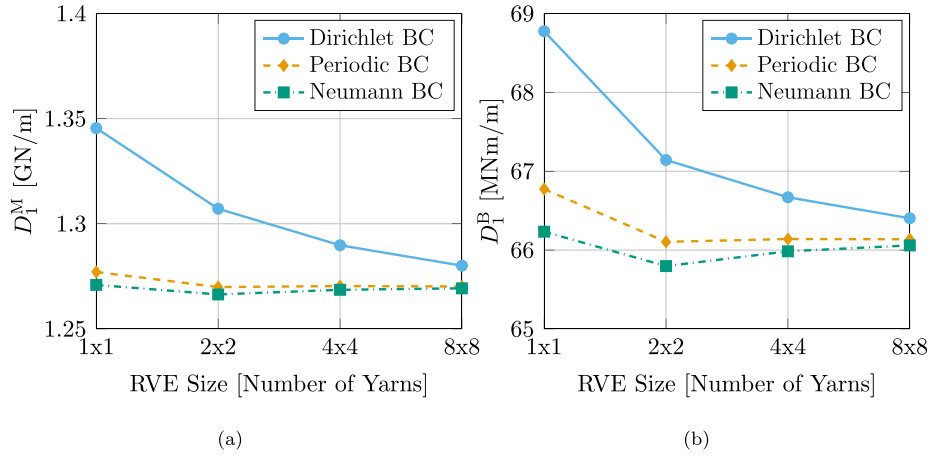
Fig. 13. The largest eigenvalue of the linear stiffness tensors, for increasing RVE size and for different boundary conditions. (a) Membrane stiffness $\bar{D}^M$. (b) Bending stiffness $\bar{D}^B$.
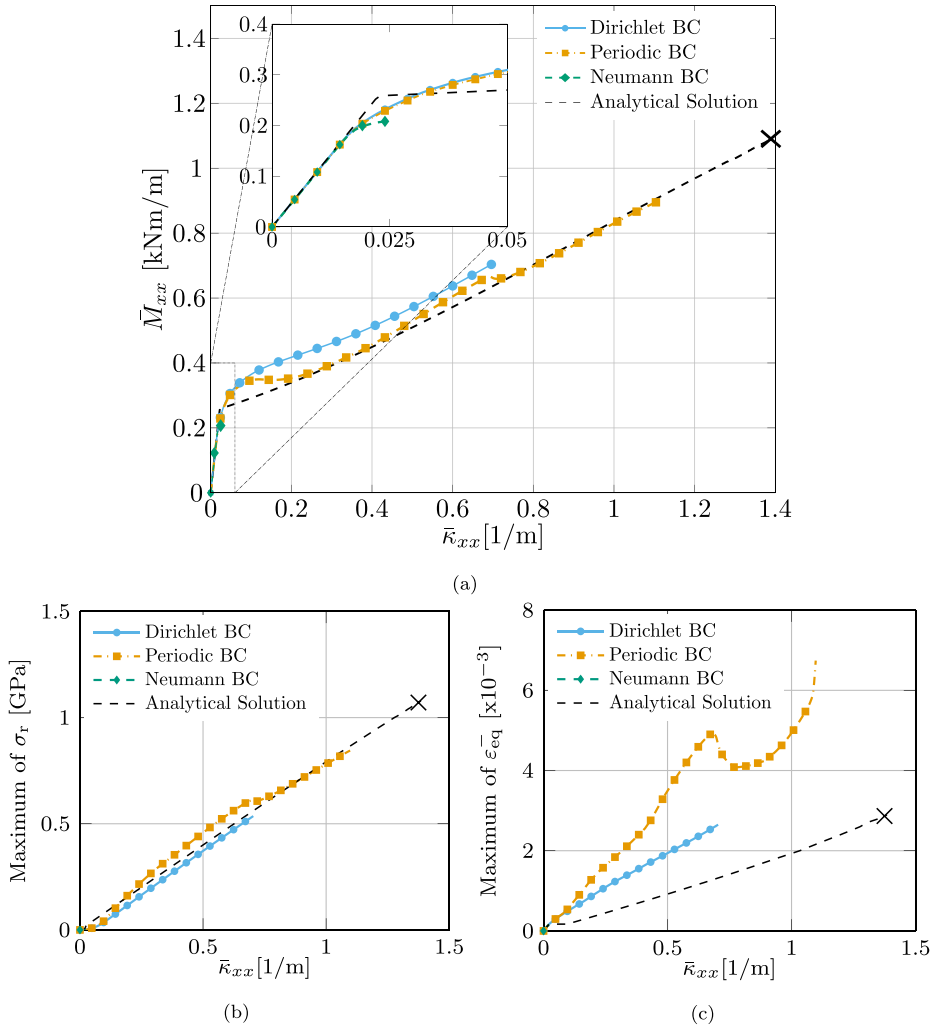

Fig. 14. Results from RVE subjected to pure uniaxial bending $\bar{\kappa}_{xx} \neq$ kNm/m ($\bar{\kappa}_{yy} = \bar{\kappa}_{xy} = 0$ 1/m and $\bar{N}_{xx} = 0$ kN/m). The numerical results are plotted up to the point where the analysis stopped converging, while the analytical solution is plotted up to the ultimate strain, marked by a cross. The ultimate compressive strain is highlighted with a cross. (a) Effective bending moment–curvature response. (b) Maximum yarn stress (c) Maximum negative equivalent strain.

does show significant tension softening, which is not captured in the simplified beam model.

To assess the failure mode of the RVE, also the maximum value of the equivalent negative strain is plotted in Fig. 14(c) and the maximum yarn stress is plotted in Fig. 14(b). The equivalent negative strain is a scalar strain metric defined as

$$\varepsilon_{eq}^- = \sqrt{\langle -\varepsilon_{el} \rangle : \langle -\varepsilon_{el} \rangle}, \tag{78}$$

where $\langle -\varepsilon_{el} \rangle$ returns the negative components of the principal strain tensor. Looking at the result in Fig. 14(b), one can observe that the
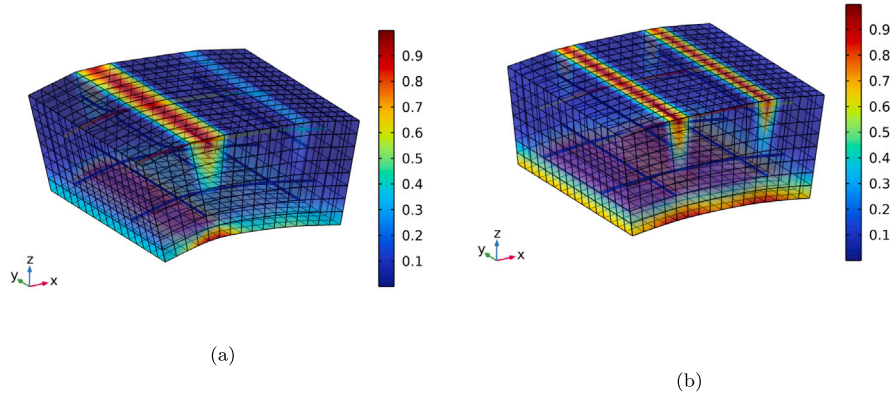
Fig. 15. Equivalent positive strain in the top half of the RVE and negative strain in the bottom half of the RVE, for the RVE subjected to uniaxial bending and using periodic boundary conditions. Both strain measures are normalized against the maximum value in the RVE. (a) At a curvature of 0.1 m^{-1}, where the strain localizes equally in the two cracks. (b) At a curvature of 0.15 m^{-1}, right after the strain localizes more in the left-most crack.

results obtained using periodic boundary conditions agree well with the analytical results. Finally, a comparison in terms of the maximum compressive strain, see Fig. 14(c) reveals that the RVE fails in compression and that the failure takes place at a smaller curvature than predicted by the beam model. From the same graph, one can also see that the strain is higher for all boundary conditions compared to the analytical solution, in particular when using the periodic boundary condition. Moreover, the predicted effective strain using periodic boundary conditions abruptly increases, first at a curvature of 0.1 m^{-1}, and then again at a curvature of 0.4 m^{-1}. This can be explained by studying the crack pattern in Fig. 15. Initially, two cracks are forming along the transverse yarns, see Fig. 15(a). But at a curvature at around 0.1 m^{-1}, a hinge starts to form at one of the cracks whereby the compressive strain in this section starts to increase rapidly.

Finally, it is of interest to study the crack patterns occurring in the simulation and to assess whether the weakening effect of the yarns actually does force strain localization. From Fig. 15, it is clear that strain localization occurs at the transverse yarns as expected. This cracking pattern has also been observed experimentally, for instance in Jesse (2004).

5.3. Validation against direct numerical simulations

To further assess and validate the performance and accuracy of the upscaling framework, especially with respect to the boundary conditions on the RVE, a comparison is made with the results from a fully resolved large-scale direct numerical simulation (DNS). In this context, the fully resolved analysis is regarded as the exact solution, while the RVE analysis is an approximation. By computing the effective strain and curvature for a subdomain of the fully resolved model and subjecting an RVE to the same loading, it is possible to measure how well the RVE predicts the response. In theory, the RVE should reproduce the effective membrane forces and moments insofar as the boundary conditions can reproduce the actual tractions and displacements on the subdomain boundary. In reality, the boundary conditions only approximate the response, and the effective response will converge to the true solution as the RVE size increases. The simulations were conducted using deformation control. Due to the highly non-linear nature of the problem, the curvature is incrementally increased from 0 to $\bar{\kappa}_{\max}$ using the parameter λ^k. In all simulations, the effective curvature $\bar{\kappa}$ is the controlled parameter. To this end, for load step k, the following strong constraint is added

$$\lambda^k \bar{\kappa}_{\max} = \left[\bar{\kappa}_{\square} \left[\boldsymbol{u}_{c,p}^k \right] \right]_{xx}. \tag{79}$$

Since $\bar{\kappa}$ is monotonically increasing for increasing λ, solving the problems using a Newton solver with constant step size is possible.
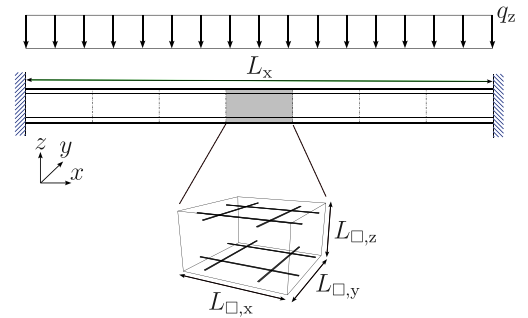

Fig. 16. Model used for the DNS of the one-way slab.

5.3.1. One-way slab

The first comparison against a DNS is done for a one-way slab, see Fig. 16. The plate is clamped in both ends and subjected to a uniformly distributed vertical force q_z. The analysis is performed for three different plate lengths and using a constant RVE size corresponding to 2×2 yarns. The action on the RVE is applied using periodic boundary conditions. Moreover, the plate is assumed to be wide enough in the y-direction so that the transverse curvature and displacement could be neglected. These assumptions make it possible to model the plate as a strip with only one RVE in the y-direction.

The effective curvature-moment response obtained from the DNS and the RVE is shown in Fig. 17(a). Overall, the result from the RVE agrees well with the DNS, with a maximum error of approximately 10% for a plate width of $9L_{\square,x}$. The error does however increase for increasing curvature as shown in Fig. 17(b), especially when the RVE starts to crack at a curvature of roughly 0.2 m^{-1}. Moreover, the error decreased when the length of the plate increased. This tendency can be explained by the fact that the separation of scales increases, i.e. that the RVE size decreases with respect to the length-scale of the plate. As the separation of scales increases, the assumption of periodic displacements becomes more accurate, and the error associated with prolongation becomes less significant.

5.3.2. Two-way slab

The same type of comparison is also done for a two-way slab, to validate the response under bi-axial bending. The setup of the analysis is shown in Fig. 18. Just as for the one-way slab, the plate consists of multiple joined sub-domains, in this case five in each direction. The plate is clamped around all vertical boundaries and is subjected to a uniform load q_z.

The result from the analysis, when using periodic boundary conditions, in terms of the effective curvature-moment response, is shown
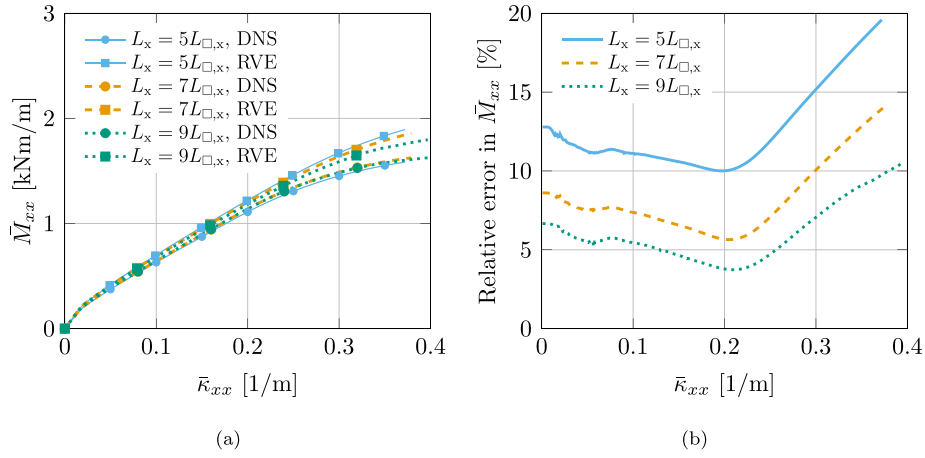
Fig. 17. Comparison of the results obtained from the DNS of a one-way slab and an RVE simulation using periodic boundary conditions. The numerical results are plotted up to the point where the maximum equivalent compressive strain reaches 2.9×10^{-3} (a) Effective bending moment–curvature response. (b) Relative error $e = M_{xx}^{RVE}/M_{xx}^{DNS} - 1$ of the effective bending moment–curvature response.
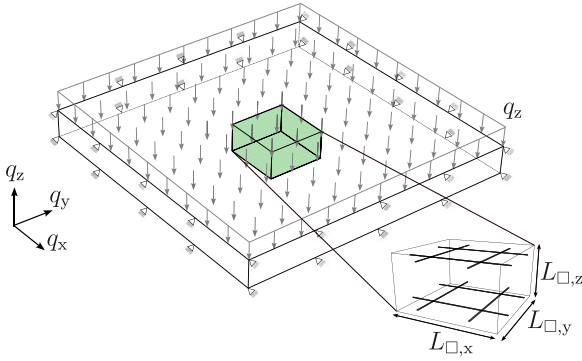

Fig. 18. Setup of the DNS of the two-way slab. The analyzed subdomain is highlighted in green.

in Fig. 19(b). Also, the bending mode and the equivalent strain for the RVE are shown in Fig. 19(a). As expected, since the plate is symmetric, the effective bending moments have the same magnitude in both directions. Additionally, in the absence of twisting, the results in the respective direction should match those in Fig. 17(a), which is clearly observed.

5.3.3. One-way slab subjected to varying external membrane force

To verify that the RVE captures the response of a plate with combined bending moment and membrane force, a DNS with an applied normal membrane force is performed for the same one-way slab as in Fig. 16. The normal stress q_x is applied at the right boundary of the plate. The right boundary is also modified to allow for an axial displacement while restricting the rotation and vertical displacement, see Fig. 20. The normal stress q_x is normalized with the plate width so that the relation between the normal traction and the maximum compressive stress from bending roughly remains constant for the different plate widths. q_x is calculated according to

$$q_x = 0.4 \frac{tL_x^2}{48 I_y} q_z, \tag{80}$$

where $I_y = \frac{t^3}{12}$ is the second moment of area per unit width of the plate and 0.4 is a scaling factor.

The result in terms of the effective curvature-moment response is shown in Fig. 21(b). The first thing to notice is the delayed cracking compared to the results from the one-way slab in Fig. 17(a). This is caused by the externally applied compressive membrane force. Also,

as for the earlier studied plate in Fig. 17(a), the error decreases with increasing separation of scales. On the other hand, the magnitude of the error is larger than for the plate with no externally applied compressive membrane force. This indicates that the RVE model is less accurate when subjected to simultaneously acting high membrane forces and bending moments. When examining the result in terms of the effective relation between the uniaxial strain and membrane force as shown in Fig. 21(a), there is no or little influence of the scale separation. This is however expected since the width of the plate has no influence on the membrane action. In general, there is a good agreement between the membrane forces computed from the RVE and the DNS.

5.3.4. One-way slab subjected to constant external membrane force

In this study, the external membrane traction is q_x constant instead of increasing with the curvature as in 5.3.3. The analysis is performed for membrane tractions corresponding to membrane forces of $\hat{N}_{xx} = 0$ kN/m, $\hat{N}_{xx} = 225$ kN/m and $\hat{N}_{xx} = 450$ kN/m and a fixed plate width of $7L_{\square,x}$. The result in terms of the effective curvature-moment response is shown in Fig. 22(a). Firstly, one can observe that the response for the case when $\hat{N}_{xx} = 0$ kN/m approximately matches that of RVE subjected to uniaxial bending, see Fig. 14(a). The reason that the graphs do not perfectly match is that the transverse curvature and strain are constrained for the DNS. Secondly, one can observe the delayed cracking and hence higher capacity that is achieved when the membrane force is increased. Lastly, the results show that the deformation capacity is drastically decreased for the case with $\hat{N}_{xx} = 450$ kN/m. This can be explained by studying the maximum equivalent compressive strain in Fig. 22(b), where it is evident that the compressive strain capacity is "consumed" by the membrane strain. There is however a positive effect of the membrane strain as can be seen for the cases when the membrane force is greater than zero, namely that the compressive strain localization caused by cracking is suppressed. Turning our attention to the normal strain-membrane force graph in Fig. 21(a), it can be observed that the plate length does not affect the membrane force. This is expected since the membrane action is statically determinate, meaning that the normal stress is determined solely by the applied membrane stress. However, local crushing of the concrete may result in local variations of the stress over the cross-section, which could explain the small deviations in membrane force observed for high strains.

6. Conclusions and outlook

In this paper, a method for scaling up the TRC response to plate membrane forces and moments was developed. The proposed method
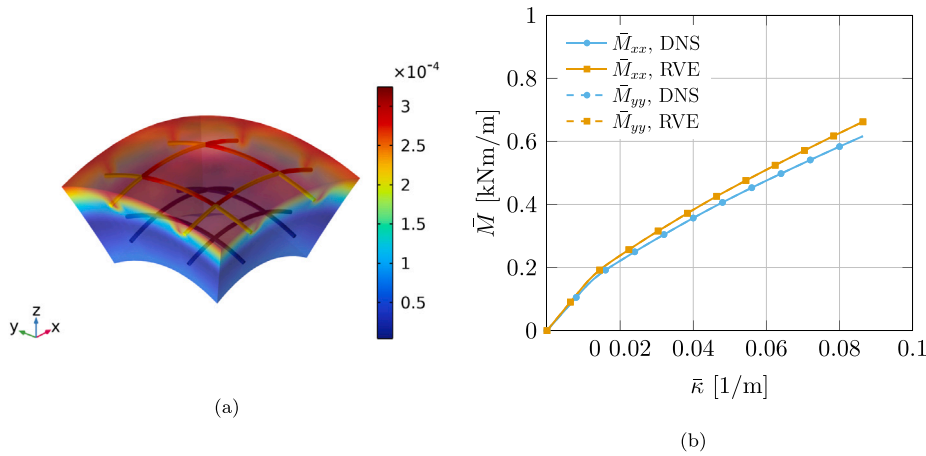
Fig. 19. Comparison of the results obtained from the DNS of a two-way slab and an RVE simulation using periodic boundary conditions. The numerical results are plotted up to the point where the analysis stopped converging due to excessive damage at the plate boundaries (a) Deformation and equivalent strain [-] for a curvature of 0.03 $1/m$ and periodic boundary conditions. (b) Effective bending moment–curvature response.
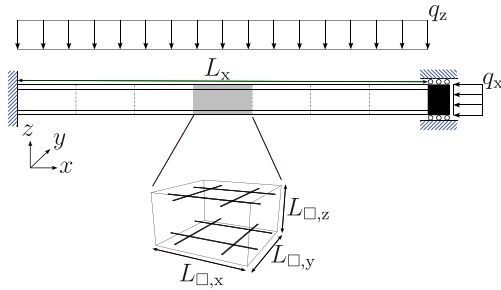

Fig. 20. Model used for the DNS of the one-way slab subjected to external membrane force.

is independent of assumptions regarding specific reinforcement layouts or material models, provided the yarns remain straight. Furthermore, the model makes it possible to capture local effects related to the interaction between the yarns and the concrete, such as bond–slip and pullout failure. By resolving the yarns, it is also possible to predict how cracks are forming and are influenced by the reinforcement layout. This makes the proposed method an option to the commonly adopted layered approach for the analysis of plates and shells when high accuracy is required and the response is highly dependent on the yarn-concrete interaction.

The effects of interfilament slip and bond–slip are captured by using efficiency factors for the strength and stiffness of the yarns. The upscaling methodology was validated against both an analytical solution and several fully resolved direct numerical simulations: one-way plates with and without applied external membrane forces, as well as a two-way plate. The results show that the RVE simulations yielded accurate results, especially for small or moderate membrane forces, with an error in the range of 5 to 20% for the studied examples. Furthermore, the accuracy was demonstrated to increase for increasing separation of scales (smaller RVEs compared to the larger scale). Three different boundary conditions were investigated: Dirichlet, Neumann and strongly periodic. Neumann and Dirichlet conditions were shown to provide lower and upper bounds, while the strongly periodic condition was shown to provide the most accurate results.

The proposed homogenization technique could be employed in large-scale plate or shell models, either by on-the-fly RVE simulations at each integration point, or by identification of a surrogate model based on virtual testing of the RVE model. For the analysis of plates, it only remains to also solve the large-scale problem in Eq. (63) together with the sub-scale problems in Eqs. (64a) and (64b). Two alternative approaches can be employed for the analysis of curved shells, either by deriving the sub-scale and large-scale problems that account for the influence of curvature, or by approximating the shell using facet shell elements. For the latter approach, it is possible to use the flat RVEs derived in this work insofar as the separation of scales is sufficient, i.e. if the influence of the curvature of the shell has little influence on the sub-scale response.

Further work could improve the accuracy of the modeling on the sub-scale. Depending on the intended application of the analysis, alternative representations of the yarns can be considered. For example, resolving the micro-structure of the yarns, as demonstrated in Voss (2008), Valeri et al. (2020) and Banholzer (2004), would make it possible to capture for instance transverse effects on the yarns or progressive failure of the yarns. It should be noted that a finer resolution in the modeling of the yarns should ideally be complemented by a more detailed representation of their geometry to account for effects such as yarn crimping. In the case that the yarns are completely resolved, tools such as TexGen or WiseTex (Sherburn, 2025; Verpoest and Lomov, 2005) could be used. However, this would require modifications to the current formulation. Currently, only straight yarns are considered, which is a reasonable simplification for plain weaves. However, for woven textiles, the curvature of the yarns has to be considered also on the sub-scale. Furthermore, to properly model 3D textiles with spacer yarns requires careful consideration of the yarn anchorage and yarn-yarn interaction. Finally, it also remains to validate all the different bending and membrane modes, especially the twisting and shear modes, as well as all combinations of the modes.

Finally, we note that the upscaling framework developed in this work could be used for two-scale optimization of TRC plates and shells. At the large scale, typical design variables are related to thickness, shape, and density (for topology optimization). The two-scale framework also incorporates design parameters at the sub-scale, such as parameters related to fiber orientation, textile architecture, and material properties for the concrete and the fibers. This approach enables a more holistic optimization of plates and shells, maximizing the potential of TRC.

CRediT authorship contribution statement

Gabriel Edefors: Writing – review & editing, Writing – original draft, Visualization, Validation, Methodology, Investigation, Formal analysis. **Fredrik Larsson:** Writing – review & editing, Supervision, Methodology, Formal analysis, Conceptualization. **Karin Lundgren:** Writing – review & editing, Supervision, Methodology, Formal analysis, Conceptualization.
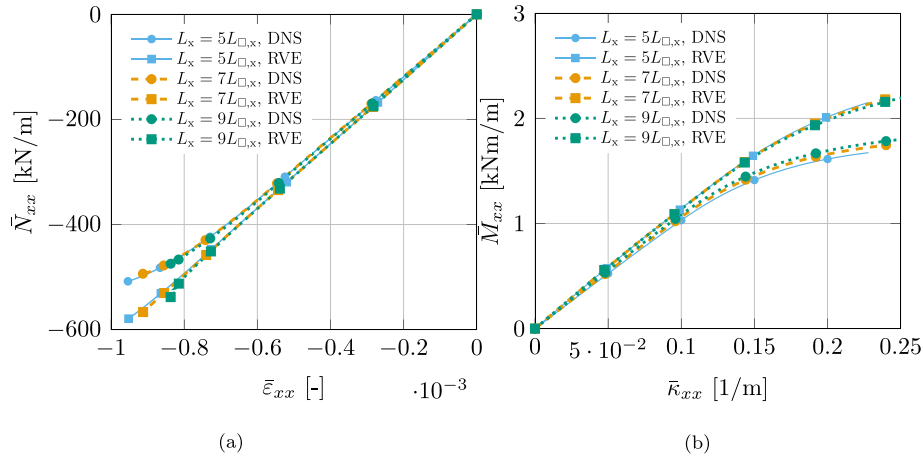
Fig. 21. Comparison of the effective RVE response and the result from the DNS of the one-way slab subjected to an external membrane force. The numerical results are plotted up to the point where the maximum equivalent compressive strain reaches 2.9×10^{-3} (a) Strain-membrane force response. (b) Curvature-moment response.
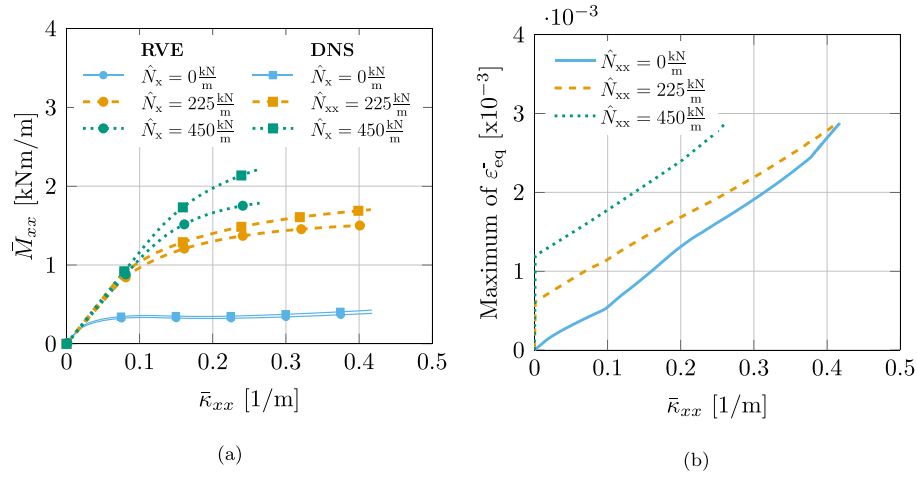

Fig. 22. Comparison of the effective RVE response and the result from the DNS of the one-way slab subjected to a prescribed membrane force $\hat{N}_{\text{xx}}$. The numerical results are plotted up to the point where the maximum equivalent compressive strain reaches 2.9×10^{-3} (a) Curvature-moment response. (b) Curvature-maximum equivalent compressive strain response measured for the RVE.

Declaration of Generative AI and AI-assisted technologies in the writing process

During the preparation of this work the authors used ChatGPT in order to improve spelling and grammar. After using this tool, the authors reviewed and edited the content as needed and take full responsibility for the content of the publication.

Declaration of competing interest

The authors declare that they have no known competing financial interests or personal relationships that could have appeared to influence the work reported in this paper.

Acknowledgments

Appendix A. Compatibility between prolongation and homogenization operators

First, the sub-scale displacement fields are additively decomposed into the large-scale part and the fluctuating part according to Eq. (35b)

$$
\mathcal{A}^* \left(\boldsymbol{u}_{\text{c,p}}, w_{\text{c}} \right) = \mathcal{A}^* \left(\boldsymbol{u}_{\text{c,p}}^{\text{L}} + \boldsymbol{u}_{\text{c,p}}^{\text{s}}, w_{\text{c}}^{\text{L}} + w_{\text{c}}^{\text{s}} \right) =
\begin{Bmatrix}
\bar{u}_{\square}[\boldsymbol{u}_{\text{c,p}}^{\text{L}} + \boldsymbol{u}_{\text{c,p}}^{\text{s}}], \\
\bar{h}_{\square}[\boldsymbol{u}_{\text{c,p}}^{\text{L}} + \boldsymbol{u}_{\text{c,p}}^{\text{s}}], \\
\bar{w}_{\square}[\boldsymbol{u}_{\text{c,p}}^{\text{L}} + \boldsymbol{u}_{\text{c,p}}^{\text{s}}, w_{\text{c}}^{\text{L}} + w_{\text{c}}^{\text{s}}], \\
\bar{\theta}_{\square}[\boldsymbol{u}_{\text{c,p}}^{\text{L}} + \boldsymbol{u}_{\text{c,p}}^{\text{s}}], \\
\bar{\kappa}_{\square}[\boldsymbol{u}_{\text{c,p}}^{\text{L}} + \boldsymbol{u}_{\text{c,p}}^{\text{s}}]
\end{Bmatrix}.
$$
(A.1)

Now, since $\mathcal{A}^*$ is a linear operator it is possible to sum the separately homogenized large-scale part and the fluctuating part

$$
\mathcal{A}^* \left(\boldsymbol{u}_{\text{c,p}}, w_{\text{c}} \right) =
\begin{Bmatrix}
\bar{u}_{\square}[\boldsymbol{u}_{\text{c,p}}^{\text{L}}] + \bar{u}_{\square}[\boldsymbol{u}_{\text{c,p}}^{\text{s}}], \\
\bar{h}_{\square}[\boldsymbol{u}_{\text{c,p}}^{\text{L}}] + \bar{h}_{\square}[\boldsymbol{u}_{\text{c,p}}^{\text{s}}], \\
\bar{w}_{\square}[\boldsymbol{u}_{\text{c,p}}^{\text{L}}, w_{\text{c}}^{\text{L}}] + \bar{w}_{\square}[\boldsymbol{u}_{\text{c,p}}^{\text{s}}, w_{\text{c}}^{\text{s}}], \\
\bar{\theta}_{\square}[\boldsymbol{u}_{\text{c,p}}^{\text{L}}] + \bar{\theta}_{\square}[\boldsymbol{u}_{\text{c,p}}^{\text{s}}], \\
\bar{\kappa}_{\square}[\boldsymbol{u}_{\text{c,p}}^{\text{L}}] + \bar{\kappa}_{\square}[\boldsymbol{u}_{\text{c,p}}^{\text{s}}]
\end{Bmatrix}
=
\begin{Bmatrix}
\bar{u}_{\square}[\boldsymbol{u}_{\text{c,p}}^{\text{L}}], \\
\bar{h}_{\square}[\boldsymbol{u}_{\text{c,p}}^{\text{L}}], \\
\bar{w}_{\square}[\boldsymbol{u}_{\text{c,p}}^{\text{L}}, w_{\text{c}}^{\text{L}}], \\
\bar{\theta}_{\square}[\boldsymbol{u}_{\text{c,p}}^{\text{L}}], \\
\bar{\kappa}_{\square}[\boldsymbol{u}_{\text{c,p}}^{\text{L}}]
\end{Bmatrix}.
$$
(A.2)

where Eq. (55) was used to remove the homogenized fluctuating sub-scale fields. Subsequently, we show the identity in Eq. (55).

A.1. Compatibility between homogenization and prolongation operators

In order to show that $\bar{u}_\square\left[u_{c,p}^L\right] = \bar{u}_p$, the prolonged field $u_{c,p}^L$ from Eq. (45) is substitute into the homogenization operator Eq. (38), whereby

$$
\bar{u}_\square\left[u_{c,p}^L\right] = \frac{1}{|\Omega_\square|}\int_{\Omega_\square}\bar{u}_{c,p} - z\bar{\theta}\left(\bar{x}_p\right) + \bar{h}(\bar{x}_p)\cdot\left[x_p - \bar{x}_p\right] -
$$
$$
z\bar{\kappa}\left(\bar{x}_p\right)\cdot\left[x_p - \bar{x}_p\right]\,\mathrm{d}\Omega = \bar{u}_p \quad \square \tag{A.3}
$$

where it was used that all terms except the one involving $\bar{u}_{c,p}$ are zero, since $\bar{\theta}$, $\bar{h}$ and $\bar{\kappa}$ are constant inside each RVE and that the average of $\left[x_p - \bar{x}_p\right]$ is also zero in each RVE.

Compatibility between the homogenization and prolongation of displacement gradient

In order to show that $\bar{h}_\square\left[u_{c,p}\right] = \bar{h}_\square\left[u_{c,p}^L\right]$, the prolonged field $u_{c,p}^L$ from Eq. (45) is substitute into the homogenization operator Eq. (39), whereby

$$
\bar{h}_\square\left[u_{c,p}^L\right] = \frac{1}{\Omega_\square}\int_{\Omega_\square}\left[u_{c,p}^L \otimes \nabla_p\right]\mathrm{d}\Omega. \tag{A.4}
$$

The gradient operator ∇_p and the integral are distributive over addition and the terms in $u_{c,p}^L$ can be evaluated individually. The first two terms vanish since the gradient of the large-scale in-plane displacements and rotations is zero within each RVE. The third term is evaluated as

$$
\frac{1}{\Omega_\square}\int_{\Omega_\square}\left[(\bar{h}\cdot\left[x_p - \bar{x}_p\right] - z\bar{\kappa}\cdot\left[x_p - \bar{x}_p\right])\otimes\nabla_p\right]\mathrm{d}\Omega = \bar{h} \quad \square. \tag{A.5}
$$

Compatibility between the homogenization and prolongation of the out-of-plane displacement fields

In order to show that $\bar{w}_\square\left[u_{c,p}, w_c\right] = \bar{w}_\square\left[u_{c,p}^L, w_c^L\right]$, the prolonged field $u_{c,p}^L$ from Eqs. (45) and (47) are substitute into the homogenization operator Eq. (40), whereby

$$
\bar{w}_\square\left[u_{c,p}^L, w_c^L\right] = \frac{1}{|\Omega_\square|}\int_{\Omega_\square}w_c^L\,\mathrm{d}\Omega -
$$
$$
\frac{1}{2|\Omega_\square|}\int_{\Omega_\square}\left[x_p - \bar{x}_p\right]\cdot\bar{\kappa}_\square[u_{c,p}^L]\cdot\left[x_p - \bar{x}_p\right]\mathrm{d}\Omega
$$
$$
= \frac{1}{|\Omega_\square|}\int_{\Omega_\square}\bar{w}\,\mathrm{d}\Omega = \bar{w} \quad \square. \tag{A.6}
$$

Compatibility between the homogenization and prolongation of the gradient of vertical displacement field

In order to show that $\bar{\theta}_\square\left[u_{c,p}\right] = \bar{\theta}_\square\left[u_{c,p}^L\right]$, the prolonged field $u_{c,p}^L$ from Eq. (45) is substitute into the homogenization operator Eq. (39), whereby

$$
\bar{\theta}_\square\left[u_{c,p}^L\right] = \frac{1}{I_\square}\int_{\Omega_\square}z u_{c,p}\mathrm{d}\Omega. \tag{A.7}
$$

The second term is the only non-zero term. This can be evaluated as

$$
\bar{\theta}_\square\left[u_{c,p}^L\right] = \frac{1}{I_\square}\int_{\Omega_\square}z^2\bar{\theta}\left(\bar{x}_p\right)\mathrm{d}\Omega = \bar{\theta} \quad \square. \tag{A.8}
$$

Compatibility between the homogenization and prolongation of curvatures

In order to show that $\bar{\kappa}_\square\left[u_{c,p}\right] = \bar{\kappa}_\square\left[u_{c,p}^L\right]$, the prolonged field $u_{c,p}^L$ from Eq. (45) is substitute into the homogenization operator Eq. (42), whereby

$$
\bar{\kappa}_\square\left[u_{c,p}^L\right] = -\frac{1}{I_\square}\int_{\Omega_\square}z\left[u_{c,p}^L \otimes \nabla_p\right]^{\mathrm{sym}}\mathrm{d}\Omega. \tag{A.9}
$$

The gradient operator ∇_p and the integral are distributive over addition and the terms in $u_{c,p}^L$ can be evaluated individually. The first two terms vanish since the gradient of the large-scale in-plane displacements and rotations is zero within each RVE. The third term is evaluated as

$$
\frac{1}{I_\square}\int_{\Omega_\square}z\left[(\bar{h}\cdot\left[x_p - \bar{x}_p\right])\otimes\nabla_p\right]^{\mathrm{sym}}\mathrm{d}\Omega = -\bar{h}^{\mathrm{sym}}\frac{1}{I_\square}\int_{\Omega_\square}z\mathrm{d}\Omega = \mathbf{0},
$$
$$\tag{A.10}$$

where it was used that the first moment of area is zero, i.e. that

$$
\int_{\Omega_\square}z\mathrm{d}\Omega = \left|A_\square\right|\int_{-L_z/2}^{L_z/2}z\mathrm{d}\Omega = 0 \tag{A.11}
$$

Similarly, for the last and only non-zero term

$$
\frac{1}{I_\square}\int_{\Omega_\square}z\left[(-z\bar{\kappa}\cdot\left[x_p - \bar{x}_p\right])\otimes\nabla_p\right]^{\mathrm{sym}}\mathrm{d}\Omega = \bar{\kappa}^{\mathrm{sym}}\frac{1}{I_\square}\int_{\Omega_\square}z^2\mathrm{d}\Omega = \bar{\kappa} \quad \square,
$$
$$\tag{A.12}$$

where it was used that the large-scale curvature tensor is symmetric.

Appendix B. Neumann curvature constraint

By using the expression for the effective curvature in Eq. (42), together with the Gauss divergence theorem, Eq. (73a) can be expanded as

$$
\bar{\kappa}_\square[u_c] = -\frac{1}{I_\square}\int_{\Omega_\square}z\left[u_{c,p}\otimes\nabla_p\right]^{\mathrm{sym}}\mathrm{d}\Omega
$$
$$
= -\frac{1}{I_\square}\int_{\Omega_\square}\frac{z}{2}\left[\frac{\partial u_{c,p,i}}{\partial x_j} + \frac{\partial u_{c,p,j}}{\partial x_i}\right]\mathrm{d}\Omega
$$
$$
= -\frac{1}{I_\square}\left[\int_{\Gamma_\square}\frac{z}{2}n_{\square,j}u_{c,p,i}\,\mathrm{d}\Gamma + \int_{\Gamma_\square}\frac{z}{2}u_{c,p,j}n_{\square,i}\,\mathrm{d}\Gamma\right], \tag{B.1}
$$

where $n_\square$ is the unit normal of the RVE boundary. Finally, the curvature constraint can be expressed in terms of the jump of the displacement field, using that $n_{\square,j}(x^+) = -n_{\square,j}\left(\varphi_{\mathrm{per}}\left(x^+\right)\right)$. Hence

$$
\frac{1}{I_\square}\left[\int_{\Gamma_\square}\frac{z}{2}n_{\square,j}u_{c,p,i}\,\mathrm{d}\Gamma + \int_{\Gamma_\square}\frac{z}{2}u_{c,p,j}n_{\square,i}\,\mathrm{d}\Gamma\right]
$$
$$
= \frac{1}{I_\square}\left[\int_{\Gamma_\square^+}\frac{z}{2}n_{\square,j}\left(u_{c,p,i} - u_{c,p,i}\left(\varphi_{\mathrm{per}}\left(x^+\right)\right)\right)\mathrm{d}\Gamma\right.
$$
$$
\left. + \int_{\Gamma_\square^+}\frac{z}{2}\left(u_{c,p,j} - u_j\left(\varphi_{\mathrm{per}}\left(x^+\right)\right)\right)n_{\square,i}\,\mathrm{d}\Gamma\right]
$$
$$
= \frac{1}{I_\square}\int_{\Gamma_\square^+}\frac{z}{2}n_{\square,j}[\![u_{c,p,i}]\!] + \frac{z}{2}n_{\square,i}[\![u_{c,p,j}]\!]\,\mathrm{d}\Gamma = 0. \tag{B.2}
$$

Note that the constraint is expressed in terms of the jump of the displacement field by using that $n_{\square,j}(x^+) = -n_{\square,j}\left(\varphi_{\mathrm{per}}\left(x^+\right)\right)$.

Appendix C. Evaluation of sub-scale derivatives of large-scale part of displacement fields

C.1. Derivative of large-scale part of yarn displacement

The derivative of the large-scale yarn displacement is evaluated as

$$
\frac{\mathrm{d}u_r^L}{\mathrm{d}l} = \frac{\mathrm{d}}{\mathrm{d}l}\left(e_1\cdot u_c^L\right) = \frac{\mathrm{d}}{\mathrm{d}l}\left(e_{1,p}\cdot u_{c,p}^L + e_{1,z}w_c^L\right)
$$
$$
= \frac{\mathrm{d}}{\mathrm{d}l}\left(e_{1,p}\cdot(\bar{u}_p - z\bar{\theta} + \bar{h}\cdot\left[x_p - \bar{x}_p\right] - z\bar{\kappa}\cdot\left[x_p - \bar{x}_p\right])\right)
$$
$$
+ \frac{\mathrm{d}}{\mathrm{d}l}\left(e_{1,z}(\bar{w} + \bar{\theta}\cdot\left[x_p - \bar{x}_p\right] + \frac{1}{2}\left[x_p - \bar{x}_p\right]\cdot\bar{\kappa}\cdot\left[x_p - \bar{x}_p\right])\right), \tag{C.1}
$$

where $e_{1,p}$ is the in-plane part of the direction vector of the yarns. By using that

$$\frac{\partial \boldsymbol{x}_p}{\partial l} = \frac{\partial}{\partial l}\left[l\boldsymbol{e}_1 - \boldsymbol{x}_0\right] = \boldsymbol{e}_1, \tag{C.2a}$$

$$\frac{\partial z}{\partial l} = e_{1,z}, \tag{C.2b}$$

(C.1) can be evaluated as

$$\frac{\mathrm{d}u_r^L}{\mathrm{d}l} = -e_{1,p}e_{1,z} \cdot \bar{\boldsymbol{\theta}} + \boldsymbol{e}_1 \otimes \boldsymbol{e}_1 : \bar{\boldsymbol{h}} - z\boldsymbol{e}_1 \otimes \boldsymbol{e}_1 : \bar{\boldsymbol{\kappa}}$$
$$- e_{1,p}e_{1,z} \cdot \boldsymbol{\kappa} \cdot [\boldsymbol{x}_p - \bar{\boldsymbol{x}}_p] + e_{1,p}e_{1,z} \cdot \bar{\boldsymbol{\theta}} + e_{1,p}e_{1,z} \cdot \boldsymbol{\kappa} \cdot [\boldsymbol{x}_p - \bar{\boldsymbol{x}}_p]$$
$$= \boldsymbol{e}_1 \otimes \boldsymbol{e}_1 : \bar{\boldsymbol{h}} - z\boldsymbol{e}_1 \otimes \boldsymbol{e}_1 : \bar{\boldsymbol{\kappa}} \tag{C.3}$$

C.2. Gradient of large-scale part of concrete displacement

The gradient of the large-scale part of the concrete displacement vector can be formulated as

$$\boldsymbol{h}_c^L = \left[\boldsymbol{u}_{c,p}^L \otimes \boldsymbol{\nabla}_p\right] + \frac{\partial u_{c,p}^L}{\partial z} \otimes \boldsymbol{e}_z + \boldsymbol{e}_z \otimes \boldsymbol{\nabla}_p w_c^L + \frac{\partial w_c^L}{\partial z}\boldsymbol{e}_z \otimes \boldsymbol{e}_z. \tag{C.4}$$

By inserting the prolongation conditions $\boldsymbol{u}_{c,p}^L$ and ∂w_c^L, Eq. (C.4) can be evaluated as

$$\boldsymbol{h}_c^L = \bar{\boldsymbol{h}} - z\bar{\boldsymbol{\kappa}} + [-\bar{\boldsymbol{\theta}} - \bar{\boldsymbol{\kappa}} \cdot [\boldsymbol{x}_p - \bar{\boldsymbol{x}}_p]] \otimes \boldsymbol{e}_z + \boldsymbol{e}_z \otimes [\bar{\boldsymbol{\theta}} + \bar{\boldsymbol{\kappa}} \cdot [\boldsymbol{x}_p - \bar{\boldsymbol{x}}_p]]. \tag{C.5}$$

C.3. Concrete strain

The concrete strain of the prolonged displacement field can be evaluated by taking the symmetric part of the gradient of the large-scale part of the concrete displacement in Eq. (C.5), i.e.

$$\boldsymbol{\varepsilon}_c(\boldsymbol{u}_c^L) = [\boldsymbol{h}_c^L]^{\mathrm{sym}} = \bar{\boldsymbol{h}}^{\mathrm{sym}} - z\bar{\boldsymbol{\kappa}}^{\mathrm{sym}} = \bar{\boldsymbol{\varepsilon}} - z\bar{\boldsymbol{\kappa}}, \tag{C.6}$$

where the symmetry of the curvature tensor has been used, i.e. that $\bar{\boldsymbol{\kappa}}^{\mathrm{sym}} = \bar{\boldsymbol{\kappa}}$.

Appendix D. Proof of effective rigid body invariance

The proof that $\bar{\boldsymbol{N}} = \bar{\boldsymbol{N}}\{\bar{\boldsymbol{\varepsilon}}, \bar{\boldsymbol{\kappa}}\}$ and $\bar{\boldsymbol{M}} = \bar{\boldsymbol{M}}\{\bar{\boldsymbol{\varepsilon}}, \bar{\boldsymbol{\kappa}}\}$ is divided into two parts. In part I, it is proven that $\boldsymbol{u}_c^s = \boldsymbol{u}_c^s\{\bar{\boldsymbol{\varepsilon}}, \bar{\boldsymbol{\kappa}}\}$ and that $u_r^s = u_r^s\{\bar{\boldsymbol{\varepsilon}}, \bar{\boldsymbol{\kappa}}\}$, using the weak form of the sub-scale problem in Eq. (64). In step II it is shown that $\bar{\boldsymbol{N}}$ and $\bar{\boldsymbol{M}}$ are functions of $\bar{\boldsymbol{\varepsilon}}, \bar{\boldsymbol{\kappa}}$, by first showing that $\bar{\boldsymbol{N}}$ and $\bar{\boldsymbol{M}}$ are only depending on $\boldsymbol{u}_c^s, u_r^s, \boldsymbol{\varepsilon}_c(\boldsymbol{u}_c^L)$ and $\boldsymbol{\varepsilon}_r(u_r^L)$.

Step I The large-scale dependency of the weak form of the sub-scale problem in Eq. (64) is in $a_{\square,c}\left(\boldsymbol{u}_c; \delta\boldsymbol{u}_c\right)$ and $a_{\square,r}\left(u_r; \delta u_r\right)$. Using that the stress tensor $\boldsymbol{\sigma}_c$ is a function of the strain tensor $\boldsymbol{\varepsilon}_c$ and using Eq. (54), these forms can be expanded as

$$a_{\square,c}\left(\boldsymbol{u}_c; \delta\boldsymbol{u}_c^s\right) = \frac{1}{|A_\square|}\int_{\Omega_\square} \boldsymbol{\sigma}_c\left(\boldsymbol{\varepsilon}_c(\boldsymbol{u}_c^L) + \boldsymbol{\varepsilon}_c(\boldsymbol{u}_c^s)\right) : \left[\delta\boldsymbol{u}_c^s \otimes \boldsymbol{\nabla}\right] \mathrm{d}\Omega, \tag{D.1a}$$

$$a_{\square,r}\left(u_r; \delta u_r^s\right) := \frac{1}{|A_\square|}\int_{\Gamma_{r,\square}} N_r\left(\varepsilon_r(u_r^L) + \varepsilon_r(u_r^s)\right)\frac{d\delta u_r^s}{dl} \mathrm{d}\Gamma. \tag{D.1b}$$

The large-scale part of the concrete strain can be evaluated as

$$\boldsymbol{\varepsilon}_c(\boldsymbol{u}_c^L) = \bar{\boldsymbol{h}}^{\mathrm{sym}} - z\bar{\boldsymbol{\kappa}}^{\mathrm{sym}}, \tag{D.2}$$

see Eq. (C.3). The large-scale part of the reinforcement strain $\varepsilon_r(\boldsymbol{u}_c^L)$ can be identified as the derivative in Eq. (C.3)

$$\varepsilon_r(\boldsymbol{u}_c^L) = \boldsymbol{e}_1 \otimes \boldsymbol{e}_1 : \bar{\boldsymbol{\varepsilon}} - z\boldsymbol{e}_1 \otimes \boldsymbol{e}_1 : \bar{\boldsymbol{\kappa}}. \tag{D.3}$$

Now, from Eqs. (C.6) and (D.3), it is possible to conclude that

$$\boldsymbol{u}_c^s = \boldsymbol{u}_c^s\{\bar{\boldsymbol{\varepsilon}}, \bar{\boldsymbol{\kappa}}\}, \tag{D.4a}$$

$$u_r^s = u_r^s\{\bar{\boldsymbol{\varepsilon}}, \bar{\boldsymbol{\kappa}}\}. \tag{D.4b}$$

Step II The membrane forces and moments are given by Eqs. (61) and (62)

$$\bar{\boldsymbol{N}} = \frac{1}{|A_\square|}\left[\int_{\Omega_\square} \boldsymbol{\sigma}_{c,p}\left(\boldsymbol{\varepsilon}_{c,p}(\boldsymbol{u}_c^L) + \boldsymbol{\varepsilon}_{c,p}(\boldsymbol{u}_c^s)\right) \mathrm{d}\Omega \right.$$
$$\left. + \int_{\Gamma_{r,\square}} N_r\left(\varepsilon_r(u_r^L) + \varepsilon_r(u_r^s)\right)\boldsymbol{e}_1 \otimes \boldsymbol{e}_1 \mathrm{d}\Gamma\right], \tag{D.5}$$

$$\bar{\boldsymbol{M}} = -\frac{1}{|A_\square|}\left[\int_{\Omega_\square} z\boldsymbol{\sigma}_{c,p}\left(\boldsymbol{\varepsilon}_{c,p}(\boldsymbol{u}_c^L) + \boldsymbol{\varepsilon}_{c,p}(\boldsymbol{u}_c^s)\right) \mathrm{d}\Omega \right.$$
$$\left. + \int_{\Gamma_{r,\square}} zN_r\left(\varepsilon_r(u_r^L) + \varepsilon_r(u_r^s)\right)\boldsymbol{e}_1 \otimes \boldsymbol{e}_1 \mathrm{d}\Gamma\right]. \tag{D.6}$$

Now since it was shown in Eqs. (C.6), (D.3) and (D.4b) that $\boldsymbol{\varepsilon}_{c,p}(\boldsymbol{u}_c^L) = \boldsymbol{\varepsilon}_{c,p}(\bar{\boldsymbol{\varepsilon}}, \bar{\boldsymbol{\kappa}})$, that $\varepsilon_r(\boldsymbol{u}_c^L) = \varepsilon_r(\bar{\boldsymbol{\varepsilon}}, \bar{\boldsymbol{\kappa}})$, that $\boldsymbol{u}_c^s = \boldsymbol{u}_c^s\{\bar{\boldsymbol{\varepsilon}}, \bar{\boldsymbol{\kappa}}\}$ and that $u_r^s = u_r^s\{\bar{\boldsymbol{\varepsilon}}, \bar{\boldsymbol{\kappa}}\}$, we can conclude that $\bar{\boldsymbol{N}} = \bar{\boldsymbol{N}}\{\bar{\boldsymbol{\varepsilon}}, \bar{\boldsymbol{\kappa}}\}$ and $\bar{\boldsymbol{M}} = \bar{\boldsymbol{M}}\{\bar{\boldsymbol{\varepsilon}}, \bar{\boldsymbol{\kappa}}\}$ □

Appendix E. Damage modeling

For the tensile damage, an exponential strain softening law is used

$$d_t(\mu) = 1 - \frac{\varepsilon_{0,t}}{\mu}\exp\left(-\frac{\mu - \varepsilon_{0,t}}{\varepsilon_f - \varepsilon_{0,t}}\right), \tag{E.1}$$

where $\varepsilon_{0,t}$ is the tensile strain threshold, computed from the uniaxial tensile strength according to $\varepsilon_{0,t} = f_{c,t}/E_c$ (Jirásek, 2011). ε_f is a material-dependent parameter that is computed from the fracture energy G_F, the tensile strength $\sigma_{c,t}$, crack-band width h_{cb} and the strain threshold $\varepsilon_{0,t}$ as

$$\varepsilon_f = \frac{G_F}{f_{c,t}h_{cb}} + \frac{\varepsilon_{0,t}}{2}. \tag{E.2}$$

μ is a state variable that keeps track of the maximum equivalent strain attained during the load history. For the equivalent strain ε_{eq}, the Euclidean norm of the positive part of the elastic strain tensor $\boldsymbol{\varepsilon}_{el}$ is used. To better capture the behavior under bi-axial compression such as in the case of two-way plates, a modified equivalent strain from Jirásek (2011) is used, where the factor γ is added to the norm. Hence the equivalent strain can be written as

$$\varepsilon_{eq} = \gamma\sqrt{\langle\boldsymbol{\varepsilon}_{el}\rangle : \langle\boldsymbol{\varepsilon}_{el}\rangle}, \tag{E.3}$$

where $\langle\cdot\rangle$ returns only the positive components of the tensor, to account for that the tensile damage only is caused by tensile strains, see COMSOL Inc. (2024) for details. In compression, the following damage evolution is used

$$d_c(\mu) = 1 - \left(1 - A_c\right)\frac{\varepsilon_{0,c}}{\mu} - A_c\exp\left(-B_c\left(\mu - \varepsilon_{0,c}\right)\right), \tag{E.4}$$

where $\varepsilon_{0,c}$ is the compressive strain threshold and A_c B_c are parameters. These parameters are calibrated so that the maximum negative value in the uniaxial stress–strain curve matches the compressive strength $f_{c,c}$ and that the stress–strain curve has a continuous derivative. The total damage variable is obtained by adding the tensile and compressive damage variables, i.e.

$$d(\mu) = \alpha_t^\beta d_t(\mu) + \alpha_c^\beta d_c(\mu), \tag{E.5}$$

where β is denoted the shear exponent. α_t and α_c are parameters that are determined from the strain-state. The scalar damage variable d is then used in Eq. (11) to compute the damaged stress.

Data availability

Data will be made available on request.

References

Banholzer, B., 2004. Bond Behaviour of a Multi-Filament Yarn Embedded in a Cementitious Matrix (Ph.D. thesis). RWTH Aachen University.

Börjesson, E., Larsson, F., Runesson, K., Remmers, J.J., Fagerström, M., 2023. Variationally consistent homogenisation of plates. Comput. Methods Appl. Mech. Engrg. 413, http://dx.doi.org/10.1016/j.cma.2023.116094.

Brameshuber, W., 2006. Textile Reinforced Concrete - State-of-the-Art Report of RILEM TC 201-TRC. Tech. Rep., RILEM.

Bruckermann, O., 2007. Zur Modellierung des Zugtragverhaltens von textilbewehrtem Beton (Ph.D. thesis). RWTH Aachen University, URL https://publications.rwth-aachen.de/record/62306.

Challagulla, K.S., Georgiades, A.V., Saha, G.C., Kalamkarov, A.L., 2008. Micromechanical analysis of grid-reinforced thin composite generally orthotropic shells. Compos. Part B: Eng. 39, 627–644. http://dx.doi.org/10.1016/j.compositesb.2007.06.005.

Chudoba, R., Sharei, E., Scholzen, A., 2016. A strain-hardening microplane damage model for thin-walled textile-reinforced concrete shells, calibration procedure, and experimental validation. Compos. Struct. 152, 913–928. http://dx.doi.org/10.1016/j.compstruct.2016.06.030.

Coenen, E.W., Kouznetsova, V.G., Geers, M.G., 2010. Computational homogenization for heterogeneous thin sheets. Internat. J. Numer. Methods Engrg. 83, 1180–1205. http://dx.doi.org/10.1002/nme.2833.

COMSOL Inc., 2024. Structural Mechanics Module User's Guide. Tech. Rep. 6.1, COMSOL Inc., URL https://www.comsol.com/documentation/6.1/structural-mechanics-module.

European Organization for Standardization, 2004. Eurocode 2 - design of concrete structures - part 1-1: General rules and rules for buildings, bridges, and civil engineering structures. Standard, 2004, European Organization for Standardization, Brussels.

Feyel, F., Chaboche, J.-L., 2000. FE2 multiscale approach for modelling the elasto-viscoplastic behaviour of long fibre SiC/Ti composite materials. Comput. Methods Appl. Mech. Engrg. 183 (3), 309–330. http://dx.doi.org/10.1016/S0045-7825(99)00224-8.

Geers, M.G., Kouznetsova, V.G., Brekelmans, W.A., 2010. Multi-scale computational homogenization: Trends and challenges. J. Comput. Appl. Math. 234, 2175–2182. http://dx.doi.org/10.1016/j.cam.2009.08.077.

Hegger, J., Voss, S., 2008. Investigations on the bearing behaviour and application potential of textile reinforced concrete. Eng. Struct. 30, 2050–2056. http://dx.doi.org/10.1016/j.engstruct.2008.01.006.

Helbig, T., Unterer, K., Kulas, C., Rempel, S., Hegger, J., 2016. Fuß - und radwegbrücke aus carbonbeton in albstadt-ebingen: Die weltweit erste ausschließlich carbonfaserbewehrte betonbrücke. Beton- Und Stahlbetonbau 111, 676–685. http://dx.doi.org/10.1002/best.201600058.

Jesse, F., 2004. Load Bearing Behaviour of Filament Yarns in a Cementitious Matrix (Ph.D. thesis). Technische Universität Dresden, URL https://nbn-resolving.org/urn:nbn:de:swb:14-1122970324369-39398.

Jirásek, M., 2011. Damage and smeared crack models. In: Hofstetter, G., Meschke, G. (Eds.), Numerical Modeling of Concrete Cracking. Springer, Vienna, pp. 1–49.

Kadi, M.E., Tysmans, T., Verbruggen, S., Vervloet, J., Munck, M.D., Wastiels, J., Hemelrijck, D.V., 2018. A layered-wise, composite modelling approach for fibre textile reinforced cementitious composites. Cem. Concr. Compos. 94, 107–115. http://dx.doi.org/10.1016/j.cemconcomp.2018.08.015.

Krüger, M., 2004. Prestressed Textile Reinforced Concrete (Ph.D. thesis). University of Stuttgart, URL http://dx.doi.org/10.18419/opus-192.

Larsson, F., Runesson, K., Su, F., 2010. Variationally consistent computational homogenization of transient heat flow. Internat. J. Numer. Methods Engrg. 81, 1659–1686. http://dx.doi.org/10.1002/nme.2747.

May, S., Michler, H., Schladitz, F., Curbach, M., 2018. Lightweight ceiling system made of carbon reinforced concrete. Struct. Concr. 19, 1862–1872. http://dx.doi.org/10.1002/suco.201700224.

Mazars, J., 1986. A description of micro- and macroscale damage of concrete structures. Eng. Fract. Mech. 25 (6), 729–737.

Mercatoris, B.C., Massart, T.J., 2011. A coupled two-scale computational scheme for the failure of periodic quasi-brittle thin planar shells and its application to masonry. Internat. J. Numer. Methods Engrg. 85, 1177–1206. http://dx.doi.org/10.1002/nme.3018.

Oskay, C., Pal, G., 2010. A multiscale failure model for analysis of thin heterogeneous plates. Int. J. Damage Mech. 19 (5), 575–610. http://dx.doi.org/10.1177/1056789509104729.

Peled, A., Bentur, A., 2000. Geometrical characteristics and efficiency of textile fabrics for reinforcing cement composites. Cem. Concr. Res. 30, 781–790. http://dx.doi.org/10.1016/S0008-8846(00)00239-8.

Petracca, M., Pelà, L., Rossi, R., Oller, S., Camata, G., Spacone, E., 2017. Multiscale computational first order homogenization of thick shells for the analysis of out-of-plane loaded masonry walls. Comput. Methods Appl. Mech. Engrg. 315, 273–301. http://dx.doi.org/10.1016/j.cma.2016.10.046.

Platen, J., Zreid, I., Kaliske, M., 2023. A nonlocal microplane approach to model textile reinforced concrete at finite deformations. Int. J. Solids Struct. 267, 112151/1–12. http://dx.doi.org/10.1016/j.ijsolstr.2023.112151.

Preinstorfer, P., Kromoser, B., Kollegger, J., 2019. Flexural behaviour of filigree slab elements made of carbon reinforced UHPC. Constr. Build. Mater. 199, 416–423. http://dx.doi.org/10.1016/j.conbuildmat.2018.12.027.

Preinstorfer, P., Yanik, S., Kirnbauer, J., Lees, J.M., Robisson, A., 2023. Cracking behaviour of textile-reinforced concrete with varying concrete cover and textile surface finish. Compos. Struct. 312, http://dx.doi.org/10.1016/j.compstruct.2023.116859.

Rampini, M.C., Zani, G., Colombo, M., di Prisco, M., 2019. Mechanical behaviour of TRC composites: Experimental and analytical approaches. Appl. Sci. 9, http://dx.doi.org/10.3390/app9071492.

Richter, M., 2005. Development of Mechanical Models for the Analytical Description of the Material Behaviour of Textile Reinforced Concrete (Ph.D. thesis). TU Dresden, URL https://nbn-resolving.org/urn:nbn:de:swb:14-1124353924615-82806.

Sciegaj, A., Almfeldt, S., Larsson, F., Lundgren, K., 2023. Textile reinforced concrete members subjected to tension, bending, and in-plane loads: Experimental study and numerical analyses. Constr. Build. Mater. 408, http://dx.doi.org/10.1016/j.conbuildmat.2023.133762.

Sciegaj, A., Grassl, P., Larsson, F., Runesson, K., Lundgren, K., 2020. Upscaling of three-dimensional reinforced concrete representative volume elements to effective beam and plate models. Int. J. Solids Struct. 202, 835–853. http://dx.doi.org/10.1016/j.ijsolstr.2020.07.006.

Sciegaj, A., Larsson, F., Lundgren, K., 2022. Experiments and calibration of a bond-slip relation and efficiency factors for textile reinforcement in concrete. Cem. Concr. Compos. 134, http://dx.doi.org/10.1016/j.cemconcomp.2022.104756.

Sharei, E., Scholzen, A., Hegger, J., Chudoba, R., 2017. Structural behavior of a lightweight, textile-reinforced concrete barrel vault shell. Compos. Struct. 171, 505–514. http://dx.doi.org/10.1016/j.compstruct.2017.03.069.

Sherburn, M., 2025. TexGen open source project. Online. Available at http://texgen.sourceforge.net/index.php/main_page. (Accessed 26 February 2025).

Unger, J.F., Eckardt, S., 2011. Multiscale modeling of concrete. Arch. Comput. Methods Eng. 18, 341–393. http://dx.doi.org/10.1007/s11831-011-9063-8.

Valeri, P., Ruiz, M.F., Muttoni, A., 2020. Tensile response of textile reinforced concrete. Constr. Build. Mater. 258, http://dx.doi.org/10.1016/j.conbuildmat.2020.119517.

Verpoest, I., Lomov, S.V., 2005. Virtual textile composites software WiseTex: Integration with micro-mechanical, permeability and structural analysis. Compos. Sci. Technol. 65, 2563–2574. http://dx.doi.org/10.1016/j.compscitech.2005.05.031.

Voss, S., 2008. Ingenieurmodelle zum Tragverhalten von textilbewehrtem Beton (Ph.D. thesis). RWTH Aachen University.

Yu, Q., Valeri, P., Ruiz, M.F., Muttoni, A., 2021. A consistent safety format and design approach for brittle systems and application to textile reinforced concrete structures. Eng. Struct. 249, http://dx.doi.org/10.1016/j.engstruct.2021.113306.

Yvonnet, J., 2019. Computational Homogenization of Heterogeneous Materials with Finite Elements, vol. 258, Springer International Publishing, Cham, http://dx.doi.org/10.1007/978-3-030-18383-7.

Zastrau, B., Lepenies, I.G., Richter, M., 2008. On the multi scale modeling of textile reinforced concrete. Tech. Mech. 1, 53–63.